A delta-tubulin/epsilon-tubulin/Ted protein complex is required for centriole architecture

Rachel Pudlowski[1], Lingyi Xu[1], Ljiljana Milenkovic[2], Chandan Kumar[1], Katherine Hemsworth[1], Zayd Aqrabawi[1], Tim Stearns[2,3], Jennifer T. Wang[1,*]

1 - Department of Biology, Washington University in St. Louis
2 - Department of Biology, Stanford University
3 - Rockefeller University
* - Corresponding author

Abstract

Centrioles have a unique, conserved architecture formed by three linked “triplet” microtubules arranged in nine-fold symmetry. The mechanisms by which these triplet microtubules are formed are not understood and likely involve the noncanonical tubulins delta-tubulin and epsilon-tubulin. Previously, we found that human cells deficient in delta-tubulin or epsilon-tubulin form abnormal centrioles, characterized by an absence of triplet microtubules, lack of central core protein POC5, and a futile cycle of centriole formation and disintegration (Wang et al., 2017). Here, we show that human cells lacking either of the associated proteins TEDC1 and TEDC2 have these same phenotypes. Using ultrastructure expansion microscopy, we find that mutant centrioles elongate to the same length as control centrioles in G2-phase. These mutants fail to recruit inner scaffold proteins of the central core and have an expanded proximal region. During mitosis, the mutant centrioles elongate further before fragmenting and disintegrating. All four proteins physically interact and TEDC1 and TEDC2 are capable forming a subcomplex in the absence of the tubulins. These results support an AlphaFold Multimer model of the tetramer in which delta-tubulin and epsilon-tubulin are predicted to form a heterodimer. TEDC1 and TEDC2 localize to centrosomes and are mutually dependent on each other and on delta-tubulin and epsilon-tubulin for localization. Our results demonstrate that delta-tubulin, epsilon-tubulin, TEDC1, and TEDC2 function together to promote robust centriole architecture. This work also lays the groundwork for future molecular studies of this complex, providing a basis for determining the mechanisms that underlie the assembly and interplay between the triplet microtubules and inner centriole structure.

Introduction

The major microtubule organizing center of mammalian cells, the centrosome, is composed of two barrel-shaped centrioles surrounded by layers of pericentriolar material (Breslow and Holland, 2019). The unique architecture of the centriole is highly conserved: the centriole barrel walls of approximately 250 nm in diameter by 500 nm in length are formed of compound microtubules linked to each other through shared protofilament walls, arranged in nine-fold symmetry (Wang and Stearns, 2017). Centrioles exhibit proximal-distal polarity comprised of three subdomains: the proximal end with triplet microtubules, the distal end with doublet microtubules, and the central core spanning the two regions (LeGuennec et al., 2021). The triplet microtubules are named the A-, B-, and C-tubules. The A-tubule is a complete microtubule formed of 13 protofilaments, and the B- and C-tubules are partial tubules and share protofilament walls with adjacent tubules. The A- and B-tubules extend beyond the C-tubule to form the doublet microtubules of the centriole distal end. During ciliogenesis, the A- and B-tubules elongate further to form the ciliary axoneme (Wang and Stearns, 2017).

Compound microtubules are unique to centrioles and ciliary axonemes and are conserved in almost all organisms with these organelles. Little is known about the mechanisms by which they form, or the functional roles they play within centrioles and cilia. Two non-canonical members of the tubulin superfamily, delta-tubulin (TUBD1) and epsilon-tubulin (TUBE1), are required for compound microtubule formation or stability in multiple organisms (de Loubresse et al., 2001; Dupuis-Williams et al., 2002; Dutcher and Trabuco, 1998; Dutcher et al., 2002; Gadelha et al., 2006; Goodenough and StClair, 1975; Ross et al., 2013; Wang et al., 2017). Previously, we showed that human cells lacking these tubulins make aberrant centrioles that only have singlet microtubules and disintegrate in mitosis, resulting in a futile cycle of centriole formation and loss every cell cycle (Wang et al., 2017). These mutant centrioles fail to recruit the distal end protein POC5, indicating that compound microtubules may be required for centriole composition. We concluded that either the compound microtubules themselves, or the proteins that they associate with, are required for centriole stability through the cell cycle. Together, these results suggest that the compound microtubules may form a unique scaffold for the protein-protein interactions that define centrosomes and cilia.

The compound microtubules are directly linked to many of the substructures at the proximal, central, and distal regions within centrioles. At the proximal end, the cartwheel, a ninefold symmetric hub and spokes made from SASS6 and associated proteins, is connected to the A-tubule through the pinhead, which has been proposed to be formed of CEP135 and CPAP (Hatzopoulos et al., 2013; Kraatz et al., 2016; Lin et al., 2013a; Sharma et al., 2016). Multiple cartwheels are stacked within the centriole lumen to a height of approximately one-third of the entire centriole length (~170 nm in human centrioles) (Klena et al., 2020). The A-tubule of one triplet is connected to the C-tubule of the adjacent triplet through a structure known as the A-C linker. Recently CCDC77, WDR67, and MIIP were identified to be components of the A-C linkers (Bournonville et al., 2024; Laporte et al., 2024). Within the central core, a helical inner scaffold imparts structural integrity upon the centriole (Le Guennec et al., 2020; Steib et al., 2020), and recruits proteins, including gamma-tubulin, to the lumen of the centriole (Schweizer

et al., 2021). This scaffold is formed in G2-phase of the first cell cycle after centriole birth, is composed of POC5, POC1B, FAM161A, WDR90, and CCDC15 and contacts all three (A-, B-, and C-) tubules of the triplet (Arslanhan et al., 2023; Laporte et al., 2024; Le Guennec et al., 2020; Steib et al., 2020). The distal region of centrioles also has a unique protein composition, including the proteins centrin, CP110, SFI1, CEP97, CEP90, OFD1, and MNR (Kleylein-Sohn et al., 2007; Kumar et al., 2021; Laporte et al., 2022; Laporte et al., 2024; Le Borgne et al., 2022; Spektor et al., 2007). The connections between the compound microtubules and these distal end proteins are not well-understood.

Canonically, centriole formation in cycling cells is "templated," in which one newly formed procentriole is created at the proximal end of each pre-existing parental centriole in S-phase, resulting in four centrioles within the cell. During the first cycle after their formation, procentrioles acquire post-translational modifications, elongate, recruit the inner scaffold, lose the cartwheel, and undergo centriole-to-centrosome conversion. Additional changes occur during the second cell cycle, including acquisition of the distal and subdistal appendages that are important for ciliogenesis (Sullenberger et al., 2020; Tischer et al., 2021). Under experimental manipulations in which the parental centrioles are ablated, centrioles can also form *de novo* in S-phase. *De novo* centriole formation can result in more than five centrioles per cell and has been shown to be error-prone (Wang et al., 2015), perhaps indicating differences in centriole structure or regulation. The composition and architecture of centrioles made in this manner has not been systematically characterized.

Here, we extend our original work by defining the roles of two additional proteins, TEDC1 and TEDC2, that regulate triplet microtubule formation and stability. These proteins physically interact with TUBD1 and TUBE1 (Breslow et al., 2018; Huttlin et al., 2017; Huttlin et al., 2021). Loss of *Tedc1* or *Tedc2* in 3T3 cells results in a variable distribution of centriole numbers through the cell cycle, and tagged TEDC1 localizes to centrosomes (Breslow et al., 2018). We created *TEDC1*$^{-/-}$ or *TEDC2*$^{-/-}$ mutant cells in the same background as the *TUBD1*$^{-/-}$ and *TUBE1*$^{-/-}$ mutants and found that these cells phenocopy loss of TUBD1 or TUBE1. All four proteins interact in a complex. We find that the compound microtubules are required for recruiting the helical inner scaffold and correctly positioning the proximal end. As part of our analysis, we also determine the composition and architecture of centrioles formed *de novo* and find that these are very similar to those of procentrioles formed by templated centriole duplication. Together, these results indicate that compound microtubules are required for scaffolding substructures within centrioles and maintaining centriole stability through the cell cycle.

Results

Loss of TEDC1 or TEDC2 phenocopies loss of TUBD1 or TUBE1

TEDC1 and TEDC2 have been reported to physically interact with delta-tubulin and epsilon-tubulin, and loss of either *Tedc1* or *Tedc2* in 3T3 cells results in cells with a variable number of centrioles through the cell cycle (Breslow et al., 2018). To further dissect the phenotypes of loss of *TEDC1* or *TEDC2* and directly compare to our original report on delta-tubulin and epsilon-tubulin, we used CRISPR/Cas9 to generate strong loss of function/null mutations in *TEDC1* or

TEDC2 in the same cell type and background genotype (hTERT RPE-1 *TP53*$^{-/-}$, which will be referred to as RPE-1 *p53*$^{-/-}$) as the *TUBD1*$^{-/-}$ (delta-tubulin knockout) and *TUBE1*$^{-/-}$ (epsilon-tubulin knockout) mutant cells (Fig 1 - Supp 1). By immunofluorescence staining for two centriolar proteins, centrin (CETN) and CP110, we observed that *TEDC1*$^{-/-}$ and *TEDC2*$^{-/-}$ mutant cells had similar phenotypes to each other and to *TUBD1*$^{-/-}$ and *TUBE1*$^{-/-}$ mutant cells: in an asynchronously growing culture, about half of the cells had no centrioles, and half had five or more centrioles. These phenotypes were fully rescued by expression of tagged TEDC1 (TEDC1-Halotag-3xFlag) or TEDC2 (TEDC2-V5-APEX2) (Fig 1A, Fig 1 – Supp 1).

Next, we checked whether the centrioles in *TEDC1*$^{-/-}$ and *TEDC2*$^{-/-}$ mutant cells underwent a futile cycle of centriole formation and disintegration. We synchronized cells in each stage of the cell cycle, quantified the number of cells with centrioles, and found that almost all mutant cells lacked centrioles in G0/G1 phase. Centrioles formed in S-phase and disintegrated in M (Fig 1B). The centrioles that were present in mutant cells were immature: all centrioles were positive for the procentriole marker SASS6 and negative for the mature centriole marker CEP164 (Fig 1C, 1D). We conclude that cells lacking TEDC1 or TEDC2 also undergo a futile cycle, similar to cells lacking delta-tubulin or epsilon-tubulin (Fig 1G).

We also examined the centriolar microtubule status of *TEDC1*$^{-/-}$ and *TEDC2*$^{-/-}$ mutant cells by TEM. Similar to cells lacking delta-tubulin or epsilon-tubulin, we found that centrioles in *TEDC1*$^{-/-}$ and *TEDC2*$^{-/-}$ mutant cells lacked compound microtubules and only had singlet microtubules. These centrioles had cartwheels and pinheads, but A-C linkers were not visible (Fig 1E,F, Fig 1 – Supp 2). Together, these results demonstrate that loss of TEDC1 or TEDC2 phenocopies loss of delta-tubulin or epsilon-tubulin, indicating that these proteins likely act together.

TEDC1 and TEDC2 localize to centrosomes

Next, we investigated the localization of TEDC1 and TEDC2 to determine if they may directly act on centrosomes. TEDC1 and TEDC2 are expressed at low levels in cells (Fig 1 – Supp 1), and we could not reproducibly localize the endogenous proteins with antibody staining. Instead, we localized the functional, tagged proteins in our rescue cell lines. We found that the tagged rescue constructs localize to centrosomes, (Fig 2A and 2B) and the antibodies for the tags were specific (Fig 2 - Supp Fig 1E-J). TEDC1 and TEDC2 were enriched at centrosomes in S/G2 and colocalized with SASS6, but not centrin, indicating that TEDC1 and TEDC2 may localize to newly formed procentrioles and/or the proximal ends of parental centrioles.

To analyze TEDC1 and TEDC2 localization at higher resolution, we localized our tagged rescue constructs using three methods: a super-resolution spinning disk confocal microscope with immunofluorescence microscopy (Fig 2 – Supp Fig 1A,B), ultrastructure expansion microscopy (U-ExM, (Gambarotto et al., 2019), Fig 2C, D), and a second expansion microscopy method (Kong et al., 2024, Fig 2 - Supp 1C, D). With all three methods, we observed that both proteins localize to procentrioles and the proximal ends of parental centrioles. At these regions, both proteins overlap with the centriolar microtubules. Together, these results show that TEDC1 and TEDC2 localize to centrosomes and likely directly act upon them.

TEDC1, TEDC2, TUBD1 and TUBE1 form a complex in cells

To determine how TEDC1, TEDC2, TUBD1 and TUBE1 might act together, we first determined whether they are mutually required for their localization at centrosomes. We found that TEDC1 did not localize to centrioles in the absence of TEDC2, TUBD1, or TUBE1 (Figure 3A). Likewise, TEDC2 did not localize to centrioles in the absence of TEDC1, TUBD1, or TUBE1 (Figure 3B). These results indicate that these proteins are mutually required for TEDC1 or TEDC2 localization. Furthermore, overexpression of TEDC1 or TEDC2 did not rescue the centriole phenotypes in any of the other mutants, indicating that TEDC1 and TEDC2 are not downstream effectors of TUBD1 and TUBE1 (Fig 3A and 3B).

TEDC1 and TEDC2 have previously been shown to physically interact with TUBD1 and TUBE1 (Breslow et al., 2018). To further probe the nature of this interaction, we first determined whether any of these proteins may form subcomplexes in cells. We expressed TEDC1-Halotag-3xFlag in each mutant cell line and determined whether immunoprecipitation of tagged TEDC1 could precipitate the other proteins. TEDC1-Halotag-3xFlag rescuing the *TEDC1*$^{-/-}$ mutant could precipitate TEDC2, TUBD1, and TUBE1, indicating that all four proteins physically interact. TEDC1 did not interact with epsilon-tubulin in the absence of delta-tubulin, nor did it interact with delta-tubulin in the absence of TUBE1. In the absence of TEDC2, TEDC1 did not interact with TUBD1 or TUBE1. However, in the absence of TUBD1 or TUBE1, TEDC1 and TEDC2 could still interact with each other (Fig 3C).

We performed the reciprocal experiment, in which we expressed TEDC2-V5-APEX2 in each mutant cell line and determined whether immunoprecipitation of tagged TEDC2 could precipitate the other proteins. We observed similar results as our analysis with TEDC1. TEDC2-V5-APEX2 rescuing the *TEDC2*$^{-/-}$ mutant could precipitate TEDC1, TUBD1, and TUBE1, indicating that all four proteins physically interact. TEDC2 did not interact with either tubulin in the absence of the other. In the absence of TEDC1, TEDC2 did not interact with either tubulin. However, in the absence of TUBD1 or TUBE1, TEDC2 and TEDC1 could still interact (Fig 3D).

Together, these experiments indicate that TEDC1, TEDC2, TUBD1 and TUBE1 physically interact with each other, as previously reported (Breslow et al., 2018; Huttlin et al., 2017; Huttlin et al., 2021). Furthermore, TEDC1 and TEDC2 can form a subcomplex in the absence of either tubulin.

To gain additional insight into the nature of this interaction, we used AlphaFold-Multimer (Evans et al., 2021) to predict the structure of the complex. AlphaFold-Multimer predicted that TUBD1 and TUBE1 would form a heterodimer, similar to the alpha-tubulin/beta-tubulin heterodimer, with TUBD1 at the minus-end of the heterodimer. AlphaFold also predicted that the alpha-helices of TEDC1 and TEDC2 interact with each other, and that TEDC1 and TEDC2 form an interaction surface with TUBD1. These predictions, especially at the interface between TEDC1, TEDC2, and TUBD1, yielded high confidence pLDDT and PAE scores (Fig 3E-G, Fig 3 – Supp 1A). A similar prediction was obtained with the newly released AlphaFold 3 (Abramson et al., 2024)(Fig 3 – Supp 1B). As controls, we used AlphaFold-Multimer to predict whether TEDC1 and TEDC2 might interact with alpha-tubulin and beta-tubulin, and whether similar structures would be

predicted for *Xenopus* TEDC1, TEDC2, TUBD1 and TUBE1. While AlphaFold-Multimer did not predict a high-confidence interaction for TEDC1, TEDC2, alpha- and beta-tubulin (Fig 3 - Supp 1C), it did predict a high-confidence structure for *Xenopus* TEDC1, TEDC2, TUBD1 and TUBE1, similar to that predicted for the human proteins (Fig 3 - Supp 1D).

Our pulldown experiments showed that TEDC1 and TEDC2 can interact in a subcomplex in the absence of TUBD1 or TUBE1, which supports the predicted structural model, in which TEDC1 and TEDC2 are predicted to directly interact with each other without being bridged by either tubulin. Further supporting this model, immunoprecipitation of TEDC2 identifies the other proteins in stoichiometric amounts (Breslow et al., 2018), and we previously showed that TUBD1 and TUBE1 physically interact (Wang et al., 2017). Given the size and shape of the tetrameric complex as predicted by AlphaFold-Multimer, it is possible that these may form a structural component of centrioles. Future work will be necessary to test these possibilities. Together, our experiments indicate that TEDC1, TEDC2, TUBD1 and TUBE1 physically interact in a complex and are recruited together to centrioles.

Loss of TEDC1, TEDC2, TUBD1 or TUBE1 results in centrioles with aberrant ultrastructure

Next, we determined how the loss of these proteins, and the triplet microtubules themselves, affect centriole ultrastructure and protein composition. Because centrioles are constitutively formed *de novo* every cell cycle in our mutant cells, we incorporated two controls in our analysis: procentrioles undergoing normal parental-mediated centriole duplication in control (RPE-1 *p53*$^{-/-}$) cells, and centrioles formed in RPE-1 *p53*$^{-/-}$ cells *de novo* in the first cell cycle after centrinone washout. For each of the 2 control and 4 mutant cell lines, cells were synchronized by mitotic shake off, resulting in coverslips enriched for cells in late S and G2 phases, with a minor population in M phase. Synchronized cells were then expanded using U-ExM and stained for centriolar markers.

We first tested whether the microtubules of mutant centrioles could be modified by acetylation of alpha-tubulin. During centriole formation, acetylation is thought to proceed from the proximal toward the distal end and from the A- to the C-tubules (Sahabandu et al., 2019). We found that antibodies against acetylated alpha-tubulin stained mutant centrioles well (Fig 4B), indicating that centrioles with only singlet A-tubules can be acetylated.

We next tested whether mutant centrioles were capable of elongating during the cell cycle. In our expansion gels of cells enriched in late S and G2 phases, we used PCNA to mark S-phase cells and co-stained with acetylated tubulin to mark centrioles. Similar to a recently published report, we also found a range of centriole lengths in S- and G2-phases (Laporte et al., 2024). In S-phase, centrioles were short in all conditions. In G2-phase, centrioles elongated in all conditions, and mutant centrioles reached approximately similar lengths as control centrioles (Fig 4A). By contrast, mutant centriole widths did not increase and centrioles remained narrow, as we previously reported (Fig 4 – Supp 5 and Wang et al., 2017). These results indicate that centrioles with singlet microtubules can elongate to the same overall length as control centrioles

in G2 phase. Consistent with this hypothesis, CEP120, a protein involved in regulating centriole length (Comartin et al., 2013; Lin et al., 2013b; Mahjoub et al., 2010), was present and properly localized within mutant centrioles (Fig 4 - Supp 1D).

The compound microtubules of centrioles are heavily post-translationally modified, and recent studies have indicated that each tubule may acquire different modifications (Guichard et al., 2023). We checked glutamylation, a post-translational modification thought to be restricted to the outer surface of centrioles (Guichard et al., 2023). Within *Chlamydomonas* centrioles, glutamylation is differentially distributed between each tubule: on the C-tubule at the distal end, on all 3 tubules in the central core, and on the A-tubule at the proximal end (Hamel et al., 2017). In human centrioles, polyglutamylation is enriched in the proximal and central regions, and is absent in the distal region (Gambarotto et al., 2019; Mahecic et al., 2020; Sullenberger et al., 2020). We used two antibodies to detect glutamylation: the GT335 antibody, which recognizes the glutamylation branch and thus detects all polyglutamylation, and the polyE antibody, which recognizes long polyglutamate side chains with at least 2 or 3 glutamate residues (Kann et al., 2003; Van Dijk et al., 2007). We found that mutant and control centrioles could be stained by GT335 (Fig 4C), indicating that mutant centrioles are at least mono-glutamylated. However, the polyE antibody did not label control procentrioles or *de novo* centrioles in the first cell cycle after their formation, making this antibody uninformative for our mutants (Fig 4D). These results show that centrioles with just singlet microtubules (A-tubules) can be mono-glutamylated. Moreover, similar to previous reports (Sullenberger et al., 2020), our results suggest that centriole glutamylation is a multi-step process, in which long glutamate side chains are added later during centriole maturation.

We previously demonstrated that *TUBD1*$^{-/-}$ and *TUBE1*$^{-/-}$ mutant centrioles fail to recruit the distal centriole protein POC5 (Wang et al., 2017). Using expansion microscopy, we found that *TEDC1*$^{-/-}$ and *TEDC2*$^{-/-}$ mutant centrioles also failed to recruit POC5 (Fig 4Ei). Since our original work was published, POC5 was shown to be a component of the helical inner scaffold within the central core. These results indicate that the helical inner scaffold is not properly formed in centrioles with singlet microtubules. To test the mechanisms underlying loss of POC5, we next tested whether mutant centrioles recruit WDR90, which has been proposed to localize to the inner junction between the A- and B-tubules and function in recruiting the inner scaffold (Steib et al., 2020). We found that WDR90 was not recruited to mutant centrioles, in contrast to control centrioles, in which it is recruited in G2-phase (Fig 4Eii). From these results, it is likely that mutant centrioles with singlet microtubules fail to build or stabilize the inner junction between the A- and B-tubules. In the absence of the inner junction and junctional protein WDR90, centrioles with singlet microtubules cannot form the inner scaffold. As also previously reported (Laporte et al., 2024), we failed to detect gamma-tubulin within the lumen of control or *de novo*-formed centrioles in S or G2-phase (Fig 4-Supp1E) and thus were unable to test whether gamma-tubulin, which is recruited to the lumen of centrioles by the inner scaffold, was mislocalized in mutant centrioles.

Next, we tested whether the centriole proximal end might be properly formed in mutant centrioles. We found that the centriolar cartwheel protein, SASS6, was present within the lumen

of control and mutant centrioles in S-phase. In control centrioles in G2-phase, SASS6 was restricted to just the proximal end. Surprisingly, SASS6 was elongated in all G2-phase mutant centrioles (Fig 4F, Fig 4 – Supp 4). We observed a similar phenotype with multiple other proximal-end proteins: CEP135, STIL, CPAP, and CEP44 (Fig 4G-I, Fig 4 - Supp 1, Fig 4 – Supp 3), indicating that the entire proximal end is elongated in mutant centrioles. The extended localization of proximal end proteins was not due to increased protein expression in mutant cells (Fig 4 - Supp 2). We conclude that loss of TEDC1, TEDC2, TUBD1, or TUBE1 results in elongated proximal end domains within mutant centrioles.

Elongation of the proximal end of centrioles may also indicate an overall defect in centriole polarity. To test this hypothesis, we next determined whether these mutant centrioles might properly recruit proteins to their distal ends. We found that CETN2 and CP110, two proteins of the distal centriole, were localized to mutant centrioles and clearly marked one end of the centriole barrel in both S-phase and G2-phase (Fig 4 - Supp 1B, 1C). We conclude that proximal-to-distal centriole polarity was unaffected in mutant centrioles, and proximal end elongation did not affect the recruitment of proteins to the centriole distal end. Together, these results indicate that centrioles lacking compound microtubules are unable to properly regulate the length of the proximal end.

Mutant centrioles elongate further in mitosis before fragmenting

Centrioles lacking triplet microtubules undergo a futile cycle of formation and disassembly, but the mechanisms underlying disassembly are not well-understood. We first tested whether centriole loss in mutant centrioles may be due to loss of CEP295. CEP295 promotes centriole-to-centrosome conversion, a process in which pericentriolar material is recruited to newly-formed procentrioles. Cells lacking CEP295 form centrioles that disintegrate during the cell cycle due to a failure to undergo centriole-to-centrosome conversion (Izquierdo et al., 2014). Using U-ExM, we found that CEP295 was present and normally localized within mutant centrioles in both S- and G2-phases (Fig 4 - Supp 1F). We conclude that centriole loss in our mutants is unlikely to be due to loss of CEP295 localization, and therefore that TEDC1, TEDC2, TUBD1 and TUBE1 are likely part of a different pathway required for centriole stability through the cell cycle.

Next, we used U-ExM to visualize centriole loss during mitosis. We stained for the centriole wall (GT335), the centriole proximal end (SASS6) and the centriole distal end (CP110). In control cells, in which centrioles formed *de novo* after centrinone washout, multiple centrioles could be seen throughout mitosis, and SASS6 was lost from centrioles in anaphase-stage cells (Fig 5A,B). By contrast, in prometaphase stage *TUBD1*$^{-/-}$ or *TUBE1*$^{-/-}$ cells, we found that centrioles had a unique appearance: they were longer than normal, with an elongated proximal end marked by SASS6, and a CP110-positive cap. These two ends were connected by weak monoE staining (Fig 5C, 5E). This phenotype is identical to our observations of centrioles in a prometaphase *TUBE1*$^{-/-}$ cell by TEM in our previous publication (Wang et al., 2017, Fig 2B). After metaphase, centrioles in mutant cells were either completely absent, or had a fragmented appearance (Fig 5D, 5F), with aggregates of staining that did not resemble true centrioles. We

conclude that in our mutant cells, centrioles elongate in early mitosis to form an aberrant intermediate structure, followed by fragmentation in late mitosis.

Discussion

Here, we extend our previous study on delta-tubulin (TUBD1), epsilon-tubulin (TUBE1) and the centriolar triplet microtubules. Previously, we showed that loss of either of these proteins from mammalian cultured cell lines results in the same phenotype: loss of the triplet microtubules and a futile cycle of centriole formation and disintegration (Wang et al., 2017). Here, we add two new proteins to this pathway: TEDC1 and TEDC2, which were originally identified by their association with TUBD1 and TUBE1 (Breslow et al., 2018; Huttlin et al., 2017; Huttlin et al., 2021). Loss of TEDC1 or TEDC2 phenocopies the loss of TUBD1 or TUBE1: aberrant centrioles are formed that lack triplet microtubules and disintegrate during passage through mitosis. TEDC1 and TEDC2 localize to centrioles, indicating that they have a direct role in forming or maintaining centriole structure, and their localization depends on each of the other three proteins within the complex. All four proteins physically interact with each other. Using our mutant cell lines, we interrogated whether any of these proteins can form subcomplexes within cells. We found that TEDC1 and TEDC2 can interact with each other independently of the tubulins, supporting a predicted AlphaFold-Multimer model. Together, these results indicate that these four proteins act together in a complex at centrosomes to form or stabilize the compound microtubules.

While the molecular mechanisms underlying the function of this complex are unknown, an attractive model is that the tetrameric complex forms a structural component of centrioles. Our AlphaFold models indicate that such a structure would be approximately 13 nm in length and 6 nm in width. Within procentrioles and the proximal region of the parental centriole, it is possible that these four proteins help form the A-C linker, the pinhead, or the triplet base. Recently, components of the A-C linker have been identified (Bournonville et al., 2024; Laporte et al., 2024), and three of the proteins in our complex (TEDC2, TUBD1, and TUBE1) had shared co-dependencies with A-C linker components using DepMap (Bournonville et al., 2024). The A-C linker is lost from our mutant centrioles, but it is not clear whether this is because these proteins have a direct role in forming A-C linkers or whether this reflects an indirect role of the triplet microtubules in stabilizing A-C linkers. We note that it is also possible that only some proteins of the complex, such as delta-tubulin and epsilon-tubulin, form structural components of centrioles, or that the complex may interact transiently with centrioles. Future experiments will reveal the mechanisms by which these proteins act.

Using ultrastructure expansion microscopy, we find that mutant centrioles with singlet microtubules exhibit additional major architectural defects, including absence of the inner scaffold and elongation of the proximal end. We propose that the absence of the inner scaffold arises from the loss of the B- and C-tubules within centrioles, which may serve to anchor WDR90 and/or other proteins of the inner scaffold. WDR90 has been proposed to localize to the inner junction between the A- and B-tubules and is required for recruiting other inner scaffold components (Le Guennec et al., 2020; Steib et al., 2020). We find that mutant centrioles with

singlet microtubules fail to localize WDR90, and thus speculate that the B-tubule is required to recruit or stabilize WDR90 at the inner junction. In addition, by cryo-electron tomography, the inner scaffold makes connections to all three (A-, B-, and C-) tubules. Though the identities of all the proteins that form these connections have not been determined, it is possible that mutant centrioles with only A-tubules also fail to provide anchoring sites for the other proteins within the inner scaffold. Together, these results demonstrate that the compound microtubules of centrioles are required for proper formation of the inner helical scaffold of the central core.

Mutant centrioles with singlet microtubules have an elongated proximal end that extends the entire length of the centriole, as marked by multiple proximal end markers (SASS6, CEP135, STIL, CPAP, CEP44). These results are also supported by our previous observations that by TEM, the lumen of *TUBD1*$^{-/-}$ and *TUBE1*$^{-/-}$ mutant centrioles are filled with electron-dense material (Wang et al., 2017). Little is known about the molecular mechanisms that regulate proximal end length, though centrioles from the symbiotic flagellate *Trichonympha* bear an elongated proximal region with extended cartwheel, and the doublet and singlet-bearing centrioles from *Drosophila* and *C. elegans* have cartwheels that extend the entire length of the centriole (González et al., 1998; Guichard and Gönczy, 2016; Guichard et al., 2012; Pelletier et al., 2006; Woglar et al., 2022). It is possible that the triplet microtubules, the inner scaffold, and/or the TUBD1/TUBE1/TEDC1/TEDC2 protein complex might act to limit the length of the proximal end. Recently, loss of the inner scaffold protein POC1A has been shown to result in centrioles with extended regions of some proximal proteins, including CEP44, CEP135, and CEP295, indicating that the inner scaffold regulates the extent of these proteins (Sala et al., 2024). Interestingly, unlike our mutant centrioles which have singlet microtubules, *POC1A*$^{-/-}$ mutant centrioles can form triplet microtubules and do not have extended SASS6 staining (Sala et al., 2024). This suggests that the height of the cartwheel may be regulated by the triplet microtubules. The cartwheel and centriolar microtubules have been proposed to assemble interdependently to impart ninefold symmetry upon the centriole (Hilbert et al., 2016), and it is possible that interdependent assembly also regulates the height of the cartwheel.

Many aspects of centriole architecture, including formation of the distal tip, centriole length regulation prior to mitosis, acquisition of post-translational modifications, establishment of proximal-distal polarity, and recruitment of proteins required for centriole-to-centrosome conversion, are unaffected in mutant centrioles. These results indicate that the proteins that regulate these processes can act upon the A-tubule independently of the B- and C-tubules.

Here, we also extend our previous observations of centriole loss in mutant centrioles. In most cell types, centrioles are inherited by daughter cells during each mitosis. Centriole loss is not unique to centrioles lacking compound microtubules: mammalian cells engineered to lack CEP295 also form centrioles that are lost through the cell cycle, due to an inability to undergo centriole to centrosome conversion (Izquierdo et al., 2014). Similarly, in *Drosophila* oocytes, down-regulation of Polo kinase and pericentriolar material triggers centriole elimination (Pimenta-Marques et al., 2016). We find that CEP295 is properly localized in mutant centrioles with singlet microtubules, indicating that centriole loss in this context may be independent of centriole to centrosome conversion and pericentriolar material recruitment. Using expansion

microscopy, we find that centriole loss is correlated with loss of the SASS6 cartwheel in mitosis. In this regard, mutant centrioles with singlet microtubules resemble centriole loss within *C. elegans* oocytes, in which an analogous structure to the cartwheel named the central tube is lost prior to centriole widening and subsequent loss of the centriolar microtubules (Pierron et al., 2023). In addition, centriole loss in our mutant cells occurs through a stereotyped progression of architectural changes in mitosis, starting with centriole over elongation in prometaphase and culminating with centriole fragmentation and loss. Prolonged mitotic arrest has been reported to result in centriole over elongation through Plk1 activity (Kong et al., 2020), and it is possible that a lengthened mitosis, as observed in these mutant cells and cells lacking centrioles (Farrell et al., 2024; Wang et al., 2017), may also result in over elongation of mutant centrioles with just A-tubules. In addition, we note that CPAP has an expanded domain in mutant centrioles compared to controls (Fig 4, (Vásquez-Limeta et al., 2022). CPAP is involved in slow processive microtubule growth (Sharma et al., 2016) and its loss results in centriole fragmentation (Vásquez-Limeta et al., 2022), and it is possible that CPAP mislocalization may also contribute to over elongation of these mutant centrioles. Future work will determine the molecular mechanisms by which mutant centrioles lacking triplet microtubules are disassembled through the cell cycle.

Finally, we note that mutant human centrioles lacking compound microtubules bear similarities to the centrioles of *Drosophila* and *C. elegans* embryos, which have evolved to lack triplet microtubules and have cartwheels extending the entire length of the centriole (González et al., 1998; Pelletier et al., 2006; Woglar et al., 2022). Embryonic centrioles in both species are shorter than that of other organisms, and helical inner scaffolds have not been reported. In both species, these diminished centrioles participate in mitosis, can duplicate their centrioles, and serve as basal bodies for sensory cilia. We speculate that centrioles with triplet microtubules and the proteins they anchor, including the inner scaffold, may be required for centriole function in organisms with motile cilia, perhaps to help stabilize the basal body against ciliary movement. Such activity has been described for *Tetrahymena* basal bodies, and mutating an inner scaffold protein, Poc1, results in abnormal bending within basal bodies (Junker et al., 2022). Further supporting this hypothesis, *Drosophila* spermatocytes, one of the few cells within this species with motile cilia, have basal bodies with triplet microtubules (González et al., 1998). We note that these spermatocytes likely form triplet microtubules in an alternative manner, as *Drosophila* lacks delta-tubulin or epsilon-tubulin.

In conclusion, this work, along with our previously published study, identifies proteins required for the formation or maintenance of the centriolar triplet microtubules and maps the requirements of these proteins and the triplets in centriole architecture. Together, these results pave the way for deeper molecular understanding of the mechanisms by which the triplet microtubules are formed and maintained reproducibly within cells to form robust centrioles and cilia.

Figure legends

Figure 1. Loss of TEDC1 or TEDC2 phenocopies loss of delta-tubulin or epsilon-tubulin
(A) Immunofluorescence staining of control (RPE1 *TP53*$^{-/-}$), *TEDC1*$^{-/-}$ (RPE1 *TP53*$^{-/-}$; *TEDC1*$^{-/-}$), TEDC1 Rescued (RPE1 *TP53*$^{-/-}$; *TEDC1*$^{-/-}$; TEDC1-Halotag-3xflag), *TEDC2*$^{-/-}$ (RPE1 *TP53*$^{-/-}$; *TEDC2*$^{-/-}$), TEDC2 Rescued (RPE1 *TP53*$^{-/-}$; *TEDC2*$^{-/-}$; Tedc2-V5-APEX2) cells. Top row: G1 stage cells with 2 centrioles. Bottom row: S/G2 stage cells with 4 centrioles. Blue: DAPI; Yellow: Centrin (CETN); Magenta: CP110. Images are maximum projections of confocal stacks. Scale bar: 5 um **(B)** Centriole number counts of the indicated cell lines. Cells were either asynchronous, serum-starved for G0/G1, stained for PCNA for S-phase, synchronized with RO-3306 for G2/M, or mitotic figures were identified by DAPI staining. Each condition was performed in triplicate, with n=100 cells scored for each. **(C)** Percent of all centrioles (parental, pro, and *de novo* centrioles) in indicated cell types positive for SASS6 staining. Each condition was performed in triplicate, with 200 cells scored for each. (D) Percent of all centrioles (parental, pro, and *de novo* centrioles) in indicated cell types positive for CEP164 staining. Each condition was performed in triplicate, with 100 cells scored for each. **(E)** TEM cross-section of a centriole in a G2-phase *TEDC1*$^{-/-}$ cell. Scale bar: 100 nm **(F)** TEM cross-section of a centriole in a G2-phase *TEDC2*$^{-/-}$ cell. Scale bar: 100 nm **(G)** Schematic of centriole formation and loss in control and *TEDC1*$^{-/-}$ or *TEDC2*$^{-/-}$ cells.

Figure 1 - Supplementary Figure 1. Genotyping of *TEDC1*$^{-/-}$ and *TEDC2*$^{-/-}$ mutant cell lines
(A) Gene structure of the TEDC1 locus in parental *TP53*$^{-/-}$ cells and the *TEDC1*$^{-/-}$ mutant. Green boxes: exons; blue lines: introns; red triangles: sgRNA binding sites; black arrow: translation start site. The *TEDC1*$^{-/-}$ mutant (clone 2F4) is a compound heterozygote bearing a deletion of 227 bp on one allele and a deletion of 329 bp on the other allele. In both alleles, the ATG start site is deleted and the next ATG is not in-frame. **(B)** Gene structure of the TEDC2 locus in parental *TP53*$^{-/-}$ cells and the *TEDC2*$^{-/-}$ mutant. Green boxes: exons; blue lines: introns; red triangles: sgRNA binding sites; black arrow: translation start site. The *TEDC2*$^{-/-}$ mutant (clone F5) is a compound heterozygote bearing a deletion of 19 bp on one allele flanking the ATG start site. On the other allele, there is an insertion of 306 bp corresponding to a fusion between TEDC2 and the hCLHC1 gene. In both alleles, the ATG start site is deleted, the next ATG is not in-frame, and no additional ATG start sites are found. **(C)** Genotyping PCR of the Tedc1 locus in parental *TP53*$^{-/-}$ cells, the *TEDC1*$^{-/-}$ mutant, and TEDC1 Rescued (RPE1 *TP53*$^{-/-}$; *TEDC1*$^{-/-}$; TEDC1-Halotag-3xflag) cells. Top: PCR for TEDC1. Bottom: PCR for Halotag. **(D)** Genotyping PCR of the TEDC2 locus in parental *TP53*$^{-/-}$ cells, the *TEDC1*$^{-/-}$ mutant, and TEDC2 Rescued (RPE1 *TP53*$^{-/-}$; *TEDC2*$^{-/-}$; TEDC2-V5-APEX2) cells. Top: PCR for TEDC2. Bottom: PCR for APEX2. **(E)** Western blot of TEDC1 protein levels in parental *TP53*$^{-/-}$ cells, the *TEDC1*$^{-/-}$ mutant, and TEDC1 Rescued (RPE1 *TP53*$^{-/-}$; *TEDC1*$^{-/-}$; TEDC1-Halotag-3xflag) cells. Total protein stain is used as a loading control. TEDC1-Halotag-3xFlag is overexpressed 73-fold above endogenous levels (average of 3 independent experiments). Asterisks mark non-specific bands. **(F)** Western blot of TEDC2 protein levels in parental *TP53*$^{-/-}$ cells, the *TEDC2*$^{-/-}$ mutant, and TEDC2 Rescued (RPE1 *TP53*$^{-/-}$; *TEDC2*$^{-/-}$; TEDC2-V5-APEX2) cells. Total protein stain is used as a loading control. TEDC2-V5-APEX2 is overexpressed 26-fold above endogenous levels (average of 3 independent experiments). Asterisks mark non-specific bands.

Figure 1 - Supplementary Figure 2. Symmetrization of *TEDC1*$^{-/-}$ and *TEDC2*$^{-/-}$ mutant centrioles

Original (left) and symmetrized (right) images of TEM images of *TEDC1*$^{-/-}$ and *TEDC2*$^{-/-}$ centrioles. The first image is the same as that in Fig 1E, the last image is the same as that in Fig 1F. The middle image is an additional centriole from the *TEDC1*$^{-/-}$ mutant cells.

Figure 2. Tedc1 and Tedc2 localize to centrioles

(A) Immunofluorescence staining of Tedc1 rescue cell lines expressing TEDC1-Halotag-3xFlag in G1, S/G2, and M. Images are maximum projections of confocal stacks. Blue: DAPI; Cyan: Centrin; Magenta: TEDC1-Halotag-3xFlag (localized with anti-Flag antibody); Yellow: SASS6. Scale bar: 5 um. **(B)** Immunofluorescence staining of Tedc2 rescue cell lines expressing TEDC2-V5-APEX2 in G1, S/G2, and M. Images are maximum projections of confocal stacks. Blue: DAPI; Cyan: Centrin (localized with anti-GFP antibody recognizing GFP-centrin); Magenta: TEDC2-V5-APEX2 (localized with anti-V5 antibody); Yellow: SASS6. Scale bar: 5 um. **(C)** U-ExM of Tedc1 rescue cell lines expressing TEDC1-Halotag-3xFlag, arranged by procentriole length. Cyan: Acetylated tubulin; Magenta: TEDC1-Halotag-3xFlag (localized with anti-Flag antibody). Confocal image stacks were deconvolved using Microvolution; single plane images shown. Scale bar: 1 um. **(D)** U-ExM of Tedc2 rescue cell lines expressing TEDC2-V5-APEX2, arranged by procentriole length. Cyan: Acetylated tubulin; Magenta: TEDC2-V5-APEX2 (localized with anti-V5 antibody). Confocal image stacks were acquired with a Yokogawa CSU-W1 spinning disk microscope and deconvolved using Microvolution; single plane images shown. Scale bar: 1 um.

Figure 2 - Supplementary Figure 1. Extended localization analyses of TEDC1 and TEDC2

(A) Immunofluorescence staining of a TEDC1 rescue cell in G2 phase expressing TEDC1-Halotag-3xFlag, super-resolution image using SoRA disk and 2.8x relay. Maximum projection. Cyan: Centrin (CETN); Magenta: TEDC1-Halotag-3xFlag (localized with anti Flag antibody); Yellow: SASS6. Scale bar: 0.5 um **(B)** Immunofluorescence staining of a TEDC2 rescue cell in G2 phase expressing TEDC2-V5-APEX2, super-resolution image using SoRA disk and 2.8x relay. Maximum projection. Cyan: Centrin (CETN); Magenta: TEDC2-V5-APEX2 (localized with anti V5 antibody); Yellow: SASS6. Scale bar: 0.5 um **(C)** Expansion microscopy image of TEDC1 rescue cells expressing TEDC1-Halotag-3xFlag. Expansion gel was made as described in (Kong et al., 2024). The procentriole is oriented vertically. Cyan: CEP44; Magenta: TEDC1-Halotag-3xFlag (localized with anti-Flag antibody). Deconvolved using Microvolution; maximum projection. Scale bar: 1 um. **(D)** Expansion microscopy image of TEDC2 rescue cells expressing TEDC2-V5-APEX2. Expansion gel was made as described in (Kong et al., 2024). The procentriole is oriented vertically. Cyan: CEP44; Magenta: TEDC2-V5-APEX2 (localized with anti-V5 antibody). Deconvolved using Microvolution; maximum projection of confocal stacks. Scale bar: 1 um. **(E)** Immunofluorescence staining of *TP53*$^{-/-}$ cells expressing Halotag-Flag - negative control for Fig 2A. Images are maximum projections of confocal stacks and were acquired with the same exposure settings as in Fig 2A. Blue: DAPI; Cyan: Centrin; Magenta: Flag; Yellow: SASS6. Scale bar: 5 um. **(F)** Immunofluorescence staining of *TP53*$^{-/-}$ cells expressing V5-APEX2 - negative control for Fig 2B. Images are maximum projections of

confocal stacks and were acquired with the same exposure settings as in Fig 2B. Blue: DAPI; Cyan: Centrin (localized with anti-GFP antibody recognizing GFP-centrin); Magenta: V5; Yellow: SASS6. Scale bar: 5 um. **(G)** U-ExM of *TP53*$^{-/-}$ cells expressing Halotag-Flag - negative control for Fig 2C. Cyan: Acetylated tubulin; Magenta: Flag. Confocal image stacks were deconvolved using Microvolution; single plane images shown. Images were acquired using the same parameters as Fig 2C. Scale bar: 1 um. **(H)** U-ExM of *TP53*$^{-/-}$ cells expressing V5-APEX2 - negative control for Fig 2D. Cyan: Acetylated tubulin; Magenta: V5. Confocal image stacks were deconvolved using Microvolution; single plane images shown. Images were acquired using the same parameters as Fig 2D. Scale bar: 1 um. **(I)** Expansion microscopy image of *TP53*$^{-/-}$ cells stained with Flag antibody, negative control for Fig 2 – Supp 1C. Cyan: CEP44; Magenta: Flag. Confocal image stacks were deconvolved using Microvolution; image is a maximum projection of confocal stack. Scale bar: 1 um. **(J)** Expansion microscopy image of *TP53*$^{-/-}$ stained with V5 antibody, negative control for Fig 2 – Supp 1D. Cyan: CEP44; Magenta: V5. Confocal image stacks were deconvolved using Microvolution; image is a maximum projection of confocal stack. Scale bar: 1 um.

Figure 3. TEDC1, TEDC2, TUBD1, TUBE1 form a complex in cells

(A) Centrosomal TEDC1 localization depends on TEDC2, TUBD1, TUBE1. Immunofluorescence staining of cells expressing TEDC1-Halotag-3xflag. Control cell is *TEDC1*$^{-/-}$ mutant cells rescued with TEDC1-Halotag-3xflag. Images are maximum projections of confocal stacks. Blue: DAPI; Cyan: SASS6; Magenta: TEDC1-Halotag-3xFlag (localized with anti-Flag antibody). Scale bar: 5 um. **(B) Centrosomal TEDC2 localization depends on TEDC1, TUBD1, TUBE1.** Immunofluorescence staining of cells expressing TEDC2-V5-APEX2. Control cell is TEDC2 mutant cells rescued with TEDC2-V5-APEX2. Images are maximum projections of confocal stacks. Blue: DAPI; Cyan: SASS6; Magenta: TEDC2-V5-APEX2 (localized with anti-V5 antibody). Scale bar: 5 um. **(C) TEDC1 pulls down TEDC2 in the absence of delta or epsilon-tubulin.** Western blot of input and pulldown of Halotag-Flag or TEDC2-Halotag-Flag in the indicated cell lines. IB: indicates the antibody used for immunoblotting. The proteins and their positions are labeled on the right. Asterisks mark non-specific bands. **(D) TEDC2 pulls down TEDC1 in the absence of delta or epsilon-tubulin.** Western blot of input and pulldown of TUBA1B-V5-APEX2 or TEDC2-V5-APEX2 in the indicated cell lines. IB: indicates the antibody used for immunoblotting. The proteins and their positions are labeled on the right. Asterisks mark non-specific bands. **(E)** AlphaFold-Multimer prediction of the complex **(F)** AlphaFold-Multimer prediction colored according to pLDDT. Very high: pLDDT > 90. High: 90 > pLDDT > 70. Low: 70 > pLDDT > 50. Very low: pLDDT <50 **(G)** Predicted align error of the AlphaFold Multimer prediction. Expected position error (Angstroms) is graphed.

Fig 3 - Supplementary Figure 1. AlphaFold-Multimer and AlphaFold3 predictions
(Ai) Rotated view of the AlphaFold-Multimer prediction from Fig 3E (120 degrees around the y-axis) **(Aii)** Rotated view colored according to pLDDT. Very high: pLDDT > 90. High: 90 > pLDDT > 70. Low: 70 > pLDDT > 50. Very low: pLDDT <50 **(Aiii)** Rotated view of the AlphaFold-Multimer prediction from Fig 3E (240 degrees around the y-axis) **(Aiv)** Rotated view colored according to pLDDT. Very high: pLDDT > 90. High: 90 > pLDDT > 70. Low: 70 > pLDDT > 50. Very low: pLDDT <50 **(Bi)** AlphaFold3 prediction of the complex **(Bii)** AlphaFold3 prediction colored according to pLDDT. Very high: pLDDT > 90. High: 90 > pLDDT > 70. Low: 70 > pLDDT > 50. Very low: pLDDT <50 **(Biii)** Predicted align error of the AlphaFold3 prediction. Expected position error (Angstroms) is graphed). **(Biv)** Structural alignment between the AlphaFold3 prediction (magenta) and the AlphaFold-Multimer prediction (cyan). Using ChimeraX v1.7.1 Matchmaker, the RMSD between 450 pruned atom pairs is 0.538 angstroms (across all 475 pairs: 0.979). **(Ci)** AlphaFold-Multimer prediction of TEDC1, TEDC2, TUBA1A, TUBB **(Cii)** AlphaFold-Multimer prediction from Ci) colored according to pLDDT. Very high: pLDDT > 90. High: 90 > pLDDT > 70. Low: 70 > pLDDT > 50. Very low: pLDDT <50 **(Ciii)** Predicted align error of the AlphaFold-Multimer prediction from Ci). Expected position error (Angstroms) is graphed. **(Di)** AlphaFold Multimer prediction of *Xenopus* TEDC1, TEDC2, TUBD1, TUBE1 **(Dii)** AlphaFold-Multimer prediction from Di) colored according to pLDDT. Very high: pLDDT > 90. High: 90 > pLDDT > 70. Low: 70 > pLDDT > 50. Very low: pLDDT <50 **(Diii)** Predicted align error of the AlphaFold-Multimer prediction from Di). Expected position error (Angstroms) is graphed.

Figure 4. Mutant centrioles elongate in G2 but fail to recruit central core proteins and have an expanded proximal region
(A) Lengths of expanded centrioles from cells of the indicated cell cycle stages. Lengths were adjusted for the gel expansion factors. Cells were synchronized in S/G2/M and S-phase cells were marked with PCNA. For each genotype, the differences between S and G2 phase centriole lengths are statistically significant (<0.0001, Welch's t-test). **(B)** U-ExM images of centrioles stained for alpha-tubulin and acetylated tubulin. **(C)** U-ExM of centrioles in S or G2 phase stained with monoE (GT335) antibody. **(D)** U-ExM of control centrioles in S or G2 phase stained with acetylated tubulin and polyE antibodies **(E) i)** U-ExM of centrioles in G2 phase stained with acetylated tubulin (cyan) and POC5 (magenta) antibodies. POC5 is present in the central core of control procentrioles and *de novo* centrioles and absent from mutants. **(ii)** U-ExM of centrioles in G2 phase stained with acetylated tubulin (cyan) and WDR90 (magenta) antibodies. WDR90 is present in the central core of control procentrioles and *de novo* centrioles, and absent from mutants. **(F, G, H, I)** U-ExM of centrioles in S and G2 phase stained for alpha tubulin (cyan) or acetylated tubulin (Ac.Tub, cyan) and the following antibodies in magenta: F) SASS6, G) CEP135, H) STIL, I) CPAP. In control centrioles, these proteins are limited to the proximal end. In mutant centrioles, these proteins are present at the proximal end in S phase centrioles and elongate throughout the entire centriole in G2 phase. Images were acquired with a Yokogawa CSU-W1 SoRA with 2.8x relay and deconvolved with 10 iterations using Microvolution. Scale bars: 1 um.

Figure 4 - Supplementary figure 1 - Extended analyses of mutant centriole architecture and U-ExM gel expansion factor

(A, B, C, D, E, F) U-ExM of centrioles in S and G2 phase stained for acetylated tubulin (cyan) and the following proteins in magenta: A) CEP44, B) CETN2, C) CP110, D) CEP120, E) gamma-tubulin, F) CEP295. Scale bars = 1 um. Images were acquired with a Yokogawa CSU-W1 SoRA with 2.8x relay and deconvolved with 10 iterations using Microvolution.

(G) Measurements of the widths of parental centrioles from each experiment as a readout of expansion factor, including the cell cycle analyses in Fig 4A and Fig 4B. Centriole widths were a mean of 1.0 um, corresponding to a four-fold expansion factor.

Figure 4 - Supplementary figure 2 - Total protein levels of centrosomal proteins are unchanged in mutant cells

(A) Western blot of control (RPE1 *TP53*$^{-/-}$), *TEDC1*$^{-/-}$, *TEDC2*$^{-/-}$, *TUBD1*$^{-/-}$, *TUBE1*$^{-/-}$, *SASS6*$^{-/-}$ cell lysates, immunoblotted for SASS6. Total protein stain (Revert) serves as a loading control. **(B)** Western blot of control (RPE1 *TP53*$^{-/-}$), *TEDC1*$^{-/-}$, *TEDC2*$^{-/-}$, *TUBD1*$^{-/-}$, *TUBE1*$^{-/-}$ cell lysates, immunoblotted for STIL. Total protein stain (Revert) serves as a loading control. **(C)** Western blot of control (RPE1 *TP53*$^{-/-}$), *TEDC1*$^{-/-}$, *TEDC2*$^{-/-}$, *TUBD1*$^{-/-}$, *TUBE1*$^{-/-}$ cell lysates, immunoblotted for CPAP. Total protein stain (Revert) serves as a loading control. **(D)** Western blot of control (RPE1 *TP53*$^{-/-}$), *TEDC1*$^{-/-}$, *TEDC2*$^{-/-}$, *TUBD1*$^{-/-}$, *TUBE1*$^{-/-}$ cell lysates, immunoblotted for POC5. Total protein stain (Revert) serves as a loading control.

Figure 4 - Supplementary figure 3 – Quantification of CEP135 centriolar localization through S and G2 phase

Mutant centrioles have over-elongated CEP135. A) control procentrioles, n=29 centrioles; B) *de novo* centrioles, n=42 centrioles; C) *TUBD1*$^{-/-}$, n=32 centrioles; D) *TUBE1*$^{-/-}$, n=30 centrioles; E) *TEDC1*$^{-/-}$, n=23 centrioles; F) *TEDC2*$^{-/-}$, n=36 centrioles.

For each panel, representative U-ExM images of centrioles in S and G2 phase are shown. These are the same centrioles as in Figure 4G and were stained for alpha-tubulin (cyan), acetylated tubulin (yellow), and CEP135 (magenta). Scale bars = 1 um.

Graphs: Each column represents a centriole, for which the proximal and distal positions of CEP135 (magenta), acetylated tubulin (yellow) and alpha-tubulin (cyan) are displayed. Centrioles were arranged from shortest to longest. Numbers were adjusted for expansion factor. A line of best fit was added for CEP135 position: control procentrioles (dashed), *de novo* centrioles (dotted), and mutants (solid).

Figure 4 - Supplementary figure 4 – Quantification of SASS6 centriolar localization through S and G2 phase

Mutant centrioles have over-elongated SASS6. A) control procentrioles, n=53 centrioles; B) *de novo* centrioles, n=44 centrioles; C) *TUBD1*$^{-/-}$, n=39 centrioles; D) *TUBE1*$^{-/-}$, n=44 centrioles; E) *TEDC1*$^{-/-}$, n=34 centrioles; F) *TEDC2*$^{-/-}$, n=30 centrioles.

Each column represents a centriole, for which the proximal and distal positions of SASS6 (magenta) and alpha-tubulin (cyan) are displayed. Centrioles were arranged from shortest to longest. A Numbers were adjusted for expansion factor. line of best fit was added for SASS6 position: control procentrioles (dashed), *de novo* centrioles (dotted), and mutants (solid).

Figure 4 - Supplementary figure 5 – Quantification of centriole widths and lengths
Mutant centrioles have smaller widths compared to controls. A) control procentrioles, n=82 centrioles; B) *de novo* centrioles, n=86 centrioles; C) *TUBD1*$^{-/-}$, n=64 centrioles; D) *TUBE1*$^{-/-}$, n=74 centrioles; E) *TEDC1*$^{-/-}$, n=56 centrioles; F) *TEDC2*$^{-/-}$, n=62 centrioles. Centriole widths and lengths measured by alpha-tubulin antibody are graphed, adjusted for expansion factor. A line of best fit was added (red).

Fig 5. Mutant centrioles elongate further in mitosis before fragmenting
U-ExM of centrioles stained for monoE (GT335, cyan), CP110 (yellow) and SASS6 (magenta). **(A)** A prometaphase cell with centrioles formed *de novo* **(B)** An anaphase cell with centrioles formed *de novo* **(C)** A prometaphase *TUBD1*$^{-/-}$ cell **(D)** A telophase *TUBD1*$^{-/-}$ cell **(E)** A prometaphase *TUBE1*$^{-/-}$ cell **(F)** An anaphase *TUBE1*$^{-/-}$ cell. Scale bars: 1 um. Images were acquired with a Yokogawa CSU-W1 SoRA with 2.8x relay.

Materials and Methods

Cell lines and cell culture

hTERT RPE-1 *TP53*$^{-/-}$ cells were a gift from Meng-Fu Bryan Tsou (Memorial Sloan Kettering Cancer Center) and were cultured in DMEM/F-12 (Corning) supplemented with 10% Cosmic Calf Serum (CCS; HyClone). HEK293T cells for lentivirus production (see below) were obtained from the ATCC and cultured in DMEM (Corning) supplemented with 10% CCS. hTERT RPE-1 and HEK293T/17 cells were authenticated using STR profiling using CODIS loci. All other cell lines used were derived from hTERT RPE-1 *TP53*$^{-/-}$ cells. Stable *TP53*$^{-/-}$*; TEDC1*$^{-/-}$ and *TP53*$^{-/-}$*; TEDC2*$^{-/-}$ knockout cell lines were made in the hTERT RPE-1 *TP53*$^{-/-}$ cells by CRISPR/Cas9 (see below). For rescue experiments, clonal knockout cell lines were rescued using lentiviral transduction (see below). All cells were cultured at 37°C under 5% CO_2, and are mycoplasma-free (Uphoff and Drexler, 2011).

Generation of *TEDC1*$^{-/-}$ and *TEDC2*$^{-/-}$ cells and rescue cell lines

TEDC1$^{-/-}$ and *TEDC2*$^{-/-}$ cells were generated by CRISPR/Cas9 mediated gene editing using a recombinantly produced, purified Cas9 protein (Cas9-NLS, QB3 Macrolab, Berkeley) and chemically synthetized two-component gRNA (crRNA:tracrRNA, Alt-R CRISPR-Cas9 system, IDT). For increased efficiency, two gRNAs, both targeting the 5' end of each gene, were used at the same time. Target sequences were: 5'-CGCCAAGTTCGACCGTCCGG-3' and 5'-CGTCCAATCACCGCACGGGC-3' for TEDC1, and 5'-CGCACAGCGACAATTGCAAT-3' and 5'-CACCGGCGCGAGCAGCCCGC-3' for TEDC2.

Lyophilized RNA oligos were reconstituted according to the instructions provided by the manufacturer (IDT). Briefly, oligos were reconstituted in the duplex buffer at a concentration of 200 µM. To anneal crRNA with tracrRNA, 3 µl of each (600 pmol) were mixed, heated to 95°C, and transferred to room temperature to gradually cool. Pre-complexed crRNA and tracrRNA (550 pmol) were mixed with purified Cas9 (360 pmol), diluted with PBS to a total volume of 25 µl and incubated for 15 min at room temperature to form ribonucloprotein complexes (RNPs).

RPE1 *TP53*$^{-/-}$ cells stably expressing GFP-centrin (Wang et al., 2017) were electroporated in a home-made electroporation buffer (Zhang et al., 2014) using Amaxa Nucleofector II (Lonza). Cells were electroporated with an equal mix of two RNPs: 50 µl of RNPs mixture was added to 2 x 10^6 cells in 200 µl electroporation buffer. To facilitate the identification of electroporated cells, an mRuby2 expressing plasmid (pcDNA3-mRuby2, plasmid pTS3994) was electroporated together with RNPs.

Two days after electroporation, cells expressing mRuby2 were sorted using FACS, and single cells were plated into 96 well plates in conditioned media. Surviving clones were genotyped by PCR of genomic DNA and screened for phenotype based on centrin-GFP expression.

Primers used for genotyping were: 5'CCCTGCCGACGCAGTGATTGG3' and 5'CAGGGAGTGGCGAGAGCACAC3' for TEDC1 and 5' CTTGCCCGCAAGGAGGGAGAGA3' and 5'GCAGGGCCCAGCCCAAACAGA3' for TEDC2.

To rescue the mutations, Halo-3xFlag-tagged TEDC1 or APEX-V5-tagged TEDC2 were introduced into the mutant cells using lentiviral transduction as described below.

Lentivirus production and viral transduction

Recombinant lentiviruses were made by cotransfection of HEK293T cells with the respective transfer vectors (TEDC1-Halotag-3xFlag and TEDC2-V5-APEX2), second-generation lentiviral cassettes (packaging vector psPAX2, pTS3312 and envelope vector pMD2.G, pTS3313) using calcium phosphate-mediated transfection. Briefly, transfection mixture was made with CaCl2, 2x HBS (50 mM Hepes, 10 mM KCl, 12 mM dextrose, 280 mM NaCl, 1.5 mM Na2HPO4x7H2O, pH 7.05), and plasmids. Cells were treated with 25 uM chloroquine immediately before transfection, then the transfection mixture was added to cells. The medium was changed 5-6 h after transfection, and viral supernatant was harvested after an additional 48 and 72 h. Recipient cells (RPE-1 *TP53*$^{-/-}$*; TEDC1*$^{-/-}$ and *TP53*$^{-/-}$*; TEDC2*$^{-/-}$ and *TP53*$^{-/-}$*; TUBD1*$^{-/-}$ and *TP53*$^{-/-}$*; TUBE1*$^{-/-}$) were transduced with viral supernatant and 8 ug/mL Sequabrene. Transduced cells were expanded to 10-cm dishes.

Immunofluorescence

Cells were grown on poly-L-lysine-coated #1.5 glass coverslips (Electron Microscopy Sciences). Cells were fixed with −20°C methanol for 15 min. Coverslips were then washed with PBS for 10 min and blocked with PBS-BT (3% BSA, 0.1% Triton X-100, 0.02% sodium azide in PBS) for 30 min. Coverslips were incubated with primary antibodies diluted in PBS-BT for 1 hr, washed with PBS-BT, incubated with secondary antibodies and DAPI diluted in PBS-BT for 1 hr, then washed again. Samples were mounted using Mowiol (Polysciences) in glycerol containing 1,4,-diazobicycli-[2.2.2]octane (DABCO, Sigma-Aldrich) antifade.

Cell cycle synchronization

For cell cycle analyses in Fig 1, cells were seeded onto coverslips, then synchronized in G0/G1 by serum withdrawal for 24 hr, or in G2 with 10 μM RO-3306 (Adipogen) for 24 hr. Cells were fixed for immunofluorescence and analyzed for centrin/CP110 presence.

For Fig 4 and 5, mitotic shakeoff was performed on asynchronously growing cells. One pre-shake was performed to improve synchronization. Cells were fixed for U-ExM and expanded as below.

Expansion microscopy

Ultrastructure Expansion Microscopy (U-ExM)

Cells were grown on poly-D-lysine-coated #1.5 glass coverslips (Electron Microscopy Sciences) and fixed with −20°C methanol for 15 min, then washed with PBS. U-ExM was performed as previously described (Gambarotto et al., 2019): coverslips were incubated overnight in an acrylamide–formaldehyde anchoring solution (AA/FA; 0.7% formaldehyde, 1% acrylamide in PBS) at 37°C. Gelation was allowed to proceed in monomer solution (19% sodium acrylate, 10% acrylamide, 0.1% bis-acrylamide, 0.5% ammonium persulfate-APS, 0.5% TEMED) for 1 hour at 37°C. Gels were heated in denaturation buffer (200 mM SDS, 200 mM NaCl, 50 mM Tris-HCl pH 9) at 95°C for 1 h. After denaturation buffer was removed, gels were washed with multiple water rinses and allowed to expand in water at room temperature overnight. Small

circles of each expanded gel (~5 mm in diameter) were excised and incubated with primary antibodies diluted in PBS-BT (3% BSA, 0.1% Triton X-100 in PBS) on a nutator at 4°C overnight. The next day, gels were washed three times with PBS-BT buffer and incubated with secondary antibodies and 5 µg/ml DAPI diluted in PBS-BT, protected from light, on a nutator at 4°C overnight.

For Fig 4, Fig 4 – Supp 3 and Fig 4 – Supp 4 when co-staining with alpha-tubulin, centrioles were fixed with 1.4% formaldehyde and 2% acrylamide for 3 to 5 hours at 37°C. U-ExM was performed as described above. Gels were pre-incubated with anti alpha-tubulin antibody at 4°C overnight prior to staining with other primary antibodies.

Expansion microscopy as per Kong et al.

For Fig 2 – Supp 1C, D, expansion microscopy was performed similar to (Kong et al., 2024). Coverslips were incubated in 4% formaldehyde in 1x PBS for 1 hour. The coverslips were then incubated overnight in an acrylamide–formaldehyde anchoring solution (AA/FA; 4% formaldehyde, 30% acrylamide in PBS) at 40°C. Gelation was allowed to proceed in monomer solution (7% sodium acrylate, 20% acrylamide, 0.04% bis-acrylamide, 0.5% ammonium persulfate-APS, 0.5% TEMED in PBS) for 20 min on ice followed by 1 hour at room temperature. Gels were heated in denaturation buffer (200 mM SDS, 200 mM NaCl, 50 mM Tris-HCl pH 9) at 90°C for 1 h. After denaturation buffer was removed, gels were washed with multiple water rinses and allowed to expand in water at room temperature overnight. Small circles of each expanded gel (~5 mm in diameter) were excised and incubated with primary antibodies diluted in PBS-BT (3% BSA, 0.1% Triton X-100 in PBS) on a nutator at 4°C overnight. The next day, gels were washed three times with PBS-BT buffer and incubated with secondary antibodies and 5 µg/ml DAPI diluted in PBS-BT, protected from light, on a nutator at 4°C overnight.

Expansion gel imaging (all protocols)

Immunostained gels were washed once with PBS and at least three times with water, and placed in a glass-bottomed 35 mm plate for imaging. All U-ExM images were acquired as *z*-stacks collected at 0.27-µm intervals using a confocal Zeiss Axio Observer microscope (Carl Zeiss) with a PlanApoChromat 1.4 NA 63× oil immersion objective, a Yokogawa CSU-W1 (Fig 2) or Yokogawa CSU-W1 SoRA head with 2.8x relay (Fig 4, 5) and a Photometrics Prime BSI express CMOS camera. Slidebook software (Intelligent Imaging Innovations, 3i) was used to control the microscope system. Deconvolution was performed with Microvolution (Cupertino, CA) using a calculated point spread function (PSF) for 10 iterations. ImageJ (FIJI) was used for image analysis (Schindelin et al., 2012).

Centriole measurements

For measuring overall centriole width or length, z-stacks of U-ExM images were measured using ImageJ (FIJI) on maximum projections. Only centrioles that were in perfect longitudinal or cross-section were measured. Three measurements were made per centriole and averaged. Measurements were adjusted for gel expansion factor. Statistical analysis was performed with Graphpad Prism.

For measuring protein position as in Fig 4 – Supp 3 and Fig 4 – Supp 4, maximum projections of U-ExM images of longitudinally positioned centrioles were measured using ImageJ (FIJI). The coordinates of the proximal-most and distal-most position for each protein were recorded. Three measurements were made per centriole and averaged. The recorded coordinates were used to

calculate the positions of the most proximal and most distal signal for each protein, then graphed from shortest to longest centriole.

Transmission electron microscopy. For ultrastructural analysis of centrosomes by TEM, RPE-1 *TP53*$^{-/-}$ *; TEDC1*$^{-/-}$ and RPE-1 *TP53*$^{-/-}$ *; TEDC2*$^{-/-}$ cells were synchronized in G2/M with 10 uM RO-3306 for 24 hrs. Cells were trypsinized, resuspended in complete media and centrifuged at 800g for 5 min. The pellet was collected in a 14-mL tube and fixed in 2% paraformaldehyde/2.5% glutaraldehyde (Ted Pella Inc., Redding, CA) in 100 mM cacodylate buffer, pH 7.2 for 2 hr at room temperature. Samples were washed in cacodylate buffer and postfixed in 1% osmium tetroxide (Ted Pella Inc.)/1.5% potassium ferricyanide (Sigma, St. Louis, MO) for 1 hr. Samples were then rinsed extensively in dH_2O prior to en bloc staining with 1% aqueous uranyl acetate (Ted Pella Inc.) for 1 hr. Following several rinses in dH_2O, samples were dehydrated in a graded series of ethanol and embedded in Eponate 12 resin (Ted Pella Inc.). Ultrathin sections of 95 nm were cut with a Leica Ultracut UCT ultramicrotome (Leica Microsystems Inc., Bannockburn, IL), stained with uranyl acetate and lead citrate, and viewed on a JEOL 1200 EX transmission electron microscope (JEOL USA Inc., Peabody, MA) equipped with an AMT 8 megapixel digital camera and AMT Image Capture Engine V602 software (Advanced Microscopy Techniques, Woburn, MA).

Symmetrization of TEM images was performed with centrioleJ (https://www.epfl.ch/labs/gonczy-lab/databases-and-resources/ressources-centriolej/).

TEDC1 and TEDC2 pulldowns

Cells stably expressing TEDC1-Halotag-3xFlag or TEDC2-V5-APEX2 were lysed in 50 mM Tris pH7.5, 150 mM NaCl, 1% Triton X-100, 1 mM DTT, Halt protease and phosphatase inhibitor cocktail (ThermoFisher Scientific) for 30 minutes on ice, then cleared by centrifugation at 21,000 g for 20 min. Protein concentration was determined by Pierce BCA Protein Assay - Reducing Agent Compatible (ThermoFisher Scientific). Each cell lysate was incubated with 25 uL of equilibrated Chromotek Halo-Trap Magnetic Agarose (Proteintech) or Chromotek V5-Trap Magnetic Agarose (Proteintech) for 1 h at 4C on a nutator. Beads were washed using a magnetic separator rack. Elution was performed by adding 80 uL of 2x SDS loading buffer (100 mM Tris pH 6.8, 4% SDS, 20% glycerol, 100 mM DTT), boiling the beads for 5 min at 95C, then separating the eluate with a magnetic separator rack. Samples were loaded on SDS-PAGE and transferred for Western blotting.

Western blotting

For Fig 4 - Supp 2, samples were lysed in 50 mM Tris pH7.5, 150 mM NaCl, 1% Triton X-100, 1 mM DTT, Halt protease and phosphatase inhibitor cocktail (ThermoFisher Scientific) for 30 minutes on ice, then cleared by centrifugation at 21,000 g for 20 min. Protein concentration was determined by Pierce BCA Protein Assay - Reducing Agent Compatible (ThermoFisher Scientific). Equal amounts of protein (20 to 40 ug) were loaded per lane. For Fig 3, samples were loaded after pulldowns.

Proteins were separated by SDS-PAGE and transferred to nitrocellulose (LiCOR Biosciences) in transfer buffer (192 mM Glycine, 25 mM Tris, 20% ethanol). Membranes were blocked with 5% milk in TBST (137 mM NaCl, 25 mM Tris, 2.7 mM KCl, 0.1% Tween-20) at room temp for 1 h, then washed three times with TBST for 5 min each wash. Membranes were incubated with primary antibodies overnight at 4C on a nutator. The next day, membranes were washed three times with TBST for 5 min each wash and incubated with secondary antibodies at room temperature for 2.5 hours. Membranes were washed again with TBST for 5 min each wash and then imaged with the LiCOR Odyssey XF imager and analyzed using Image Studio (LiCOR Biosciences). Each experiment was performed in triplicate.

Antibodies

Primary antibodies used for immunofluorescence and U-ExM and dilutions in PBS-BT: mouse IgG2b anti-acetylated-tubulin, clone 6-11B-1 (1:1000,Sigma-Aldrich Cat# T6793, RRID:AB_477585), rabbit anti-acetyl-α-tubulin (Lys40) (1:100, Cell Signaling Technology Cat# 5335, RRID:AB_10544694), mouse IgG2b anti-centrin3, clone 3e6 (1:1000, Novus Biological, RRID:AB_537701), mouse IgG2a anti-centrin, clone 20H5 (IF 1:200, UExM 1:500, EMD Millipore, RRID:AB_10563501), rat anti-Cep120 (1:1000, gift from Moe Mahjoub (Betleja et al., 2018)), rabbit anti-Cep135 (1:500, Proteintech Cat# 24428-1-AP, RRID:AB_2879543), rabbit anti-Cep295 (1:1000, Sigma-Aldrich Cat# HPA038596, RRID:AB_10672720), rabbit anti-Cep44 (1:100, Proteintech Cat# 24457-1-AP, RRID:AB_2879557), rabbit anti-CENPJ (1:500, Proteintech Cat# 11517-1-AP, RRID:AB_2244605), rabbit anti-CP110 (IF 1:200, UExM 1:2000, Proteintech Cat# 12780-1-AP, RRID:AB_10638480), mouse IgG1 anti-Flag, clone M2 (1:500, Sigma-Aldrich Cat# F1804, RRID:AB_262044), mouse IgG1 anti-gamma-tubulin, clone GTU-88 (IF 1:1000, UExM 1:500, Sigma-Aldrich, RRID:AB_477584), mouse IgG2a anti-PCNA (1:500, BioLegend, RRID:AB_314692), rabbit anti-POC5 (for IF: 1:500, Bethyl Laboratories, RRID:AB_10949152), rabbit anti-POC5 (for U-ExM: 1:500, Thermo Fisher Scientific Cat# A303-341A (also A303-341A-T), RRID:AB_10971172), mouse IgG1 anti-polyglutamylation, clone GT335 (1:500, AdipoGen Cat# AG-20B-0020, RRID:AB_2490210), rabbit anti-polyglutamate-chain, polyE (1:500, AdipoGen Cat# AG-25B-0030, RRID:AB_2490540), mouse IgG2b anti-SASS6 (1:200, Santa Cruz Cat# sc-81431, RRID:AB_1128357), rabbit anti-STIL (1:500, Abcam Cat# ab89314, RRID:AB_2197878), mouse IgG2a anti-V5 (1:00, Thermo Fisher Scientific Cat# R960-25, RRID:AB_2556564), rabbit anti-WDR90 (1:100, Thermo Fisher Scientific Cat# PA5-61943, RRID:AB_2649628), chicken anti-GFP antibody (Aves Cat #GFP-1020, RRID:AB_10000240).

For immunofluorescence and U-ExM, AlexaFluor conjugated secondary antibodies (Thermo-Fisher) were diluted 1:1000 in PBS-BT. Goat anti-Mouse IgG1, 488 (1:1000, Thermo Fisher Scientific Cat# A-21121, RRID:AB_2535764), Goat anti-Mouse IgG2a, 488 (1:1000, Thermo Fisher Scientific Cat# A-21131, RRID:AB_2535771), Goat anti-Mouse IgG2b, 488 (1:1000, Thermo Fisher Scientific Cat# A-21141, RRID:AB_2535778), Goat anti-rabbit IgG (H+L), 488 (1:1000, Thermo Fisher Scientific Cat# A-11034 (also A11034), RRID:AB_2576217), Goat anti-Mouse IgG1, 568 (1:500, Thermo Fisher Scientific Cat# A-21124, RRID:AB_2535766), Goat anti-Mouse IgG2a, 568 (1:500, Thermo Fisher Scientific Cat# A-21134, RRID:AB_2535773), Goat anti-Mouse IgG2b, 568 (1:500, Thermo Fisher Scientific Cat# A-21144,

RRID:AB_2535780), Goat anti-rabbit IgG (H+L), 568 (1:500, Thermo Fisher Scientific Cat# A-11036 (also A11036), RRID:AB_10563566), Goat anti-Mouse IgG3, 594 (1:500, Thermo Fisher Scientific Cat# A-21155, RRID:AB_2535785), Goat anti-rat IgG (H+L), 594 (1:500,Thermo Fisher Scientific Cat# A-11007 (also A11007), RRID:AB_10561522), Goat anti-Mouse IgG1, 647 (1:500, Thermo Fisher Scientific Cat# A-21240, RRID:AB_2535809), Goat anti-Mouse IgG2a, 647 (1:500, Thermo Fisher Scientific Cat# A-21241, RRID:AB_2535810), Goat anti-Mouse IgG2b, 647 (1:500, Thermo Fisher Scientific Cat# A-21242, RRID:AB_2535811), Goat anti-rabbit IgG (H+L), 647 (1:500, Thermo Fisher Scientific Cat# A32733, RRID:AB_2633282), Goat anti-Mouse, Star Red (1:200, Abberior Cat# STRED-1001, RRID:AB_3068620), Goat anti-rabbit, Star Orange (1:200, Abberior Cat #STORANGE-1002, RRID:AB_3068622), Goat anti-chicken, Alexa 488 (Thermo Fisher Scientific Cat# A-11039, RRID:AB_2534096).

Primary antibodies used for Western blotting and dilutions in TBST: rabbit anti TUBD1 (1:1000, Sigma-Aldrich Cat# HPA027090, RRID:AB_1858457), rabbit anti TUBE1 (1:1000, Sigma-Aldrich Cat # HPA032074, RRID:AB_10601216), rabbit anti C14orf80 (1:1000, Sigma-Aldrich Cat # HPA039049, RRID:AB_2676320), rabbit anti C16orf59 (1:1000, Sigma-Aldrich Cat # HPA055389, RRID:AB_2732595), mouse IgG2b anti SASS6 (1:200, Santa Cruz Biotech Cat # sc-81431, RRID:AB_1128357), rabbit anti STIL (1:2000, Abcam Cat# ab89314, RRID:AB_2197878), rabbit anti CENPJ/CPAP (1:1000, Proteintech Cat# 11517-1-AP, RRID:AB_2244605), rabbit anti POC5 (1:1000, Thermo Fisher Scientific Cat# A303-341A (also A303-341A-T), RRID:AB_10971172), mouse IgG2a anti V5 (1:1000, Thermo Fisher Scientific Cat# R960-25, RRID:AB_2556564), mouse IgG1 anti Flag, clone M2 (1:2000, Sigma-Aldrich Cat# F1804, RRID:AB_262044). Secondary antibodies used for Western blotting: 680 Donkey anti rabbit (H+L) (1:20,000, Thermo Fisher Scientific Cat# A10043, RRID:AB_2534018), 800 Donkey anti rabbit (H+L) (1:20,000, Li-COR Cat# 926-32213, RRID:AB_621848), 680 Donkey anti mouse (H+L) (1:20,000, Thermo Fisher Scientific Cat# A10038, RRID:AB_11180593), 800 Donkey anti mouse (H+L) (1:20,000, Li-COR Cat# 926-32212, RRID:AB_621847).

Acknowlegments

This work was supported by NIH/NIGMS (K99/R00 GM131024 to J.T.W. and R35 GM130286 to T.S.) and Washington University in St. Louis startup funds (to J.T.W). We thank Wandy Beatty of the Washington University Molecular Microbiology Imaging Facility for assistance with transmission electron microscopy, Moe Mahjoub (Washington University School of Medicine) for the gift of the CEP120 and goat anti-rat antibodies, and Meng-Fu Bryan Tsou (Memorial Sloan Kettering Cancer Center) for the gifts of RPE-1 *TP53*$^{-/-}$ and RPE-1 *TP53*$^{-/-}$ *; SASS6*$^{-/-}$ cells. We thank the Stanford cytoskeleton group, WashU centrosome/cilia group, members of the Stearns lab, and David Breslow for helpful discussions. We also thank Hani Zaher's and Joe Jez's labs for hosting the Wang lab during renovations and Larry Galloway for help with Python.

References

Abramson, J., Adler, J., Dunger, J., Evans, R., Green, T., Pritzel, A., Ronneberger, O., Willmore, L., Ballard, A. J., Bambrick, J., et al. (2024). Accurate structure prediction of biomolecular interactions with AlphaFold 3. *Nature* 630, 493–500.

Arslanhan, M. D., Cengiz-Emek, S., Odabasi, E., Steib, E., Hamel, V., Guichard, P. and Firat-Karalar, E. N. (2023). CCDC15 localizes to the centriole inner scaffold and controls centriole length and integrity. *Journal of Cell Biology* 222, e202305009.

Bournonville, L., Laporte, Marine. H., Borgers, S., Guichard, P. and Hamel, V. (2024). The A-C Linker controls centriole cohesion and duplication.

Breslow, D. K. and Holland, A. J. (2019). Mechanism and Regulation of Centriole and Cilium Biogenesis. *Annu. Rev. Biochem.* 88, 691–724.

Breslow, D. K., Hoogendoorn, S., Kopp, A. R., Morgens, D. W., Vu, B. K., Kennedy, M. C., Han, K., Li, A., Hess, G. T., Bassik, M. C., et al. (2018). A CRISPR-based screen for Hedgehog signaling provides insights into ciliary function and ciliopathies. *Nat Genet* 50, 460–471.

Comartin, D., Gupta, G. D., Fussner, E., Coyaud, É., Hasegan, M., Archinti, M., Cheung, S. W. T., Pinchev, D., Lawo, S., Raught, B., et al. (2013). CEP120 and SPICE1 Cooperate with CPAP in Centriole Elongation. *Current Biology* 23, 1360–1366.

de Loubresse, N. G., Ruiz, F. and Beisson, J. (2001). Role of delta-tubulin and the C-tubule in assembly of Paramecium basal bodies. *BMC Cell Biology* 7.

Dupuis-Williams, P., Fleury-Aubusson, A., de Loubresse, N. G., Geoffroy, H., Vayssié, L., Galvani, A., Espigat, A. and Rossier, J. (2002). Functional role of ε-tubulin in the assembly of the centriolar microtubule scaffold. *Journal of Cell Biology* 158, 1183–1193.

Dutcher, S. K. and Trabuco, E. C. (1998). The UNI3 Gene Is Required for Assembly of Basal Bodies of Chlamydomonas and Encodes ʕ-Tubulin, a New Member of the Tubulin Superfamily. *Molecular Biology of the Cell* 9, 16.

Dutcher, S. K., Morrissette, N. S., Preble, A. M., Rackley, C. and Stanga, J. (2002). ♪-Tubulin Is an Essential Component of the Centriole. *Molecular Biology of the Cell* 13, 11.

Evans, R., O'Neill, M., Pritzel, A., Antropova, N., Senior, A., Green, T., Žídek, A., Bates, R., Blackwell, S., Yim, J., et al. (2021). *Protein complex prediction with AlphaFold-Multimer*. Bioinformatics.

Farrell, K., Wang, J. T. and Stearns, T. (2024). Spindle assembly checkpoint-dependent mitotic delay is required for cell division in absence of centrosomes.

Gadelha, C., Wickstead, B., McKean, P. G. and Gull, K. (2006). Basal body and flagellum mutants reveal a rotational constraint of the central pair microtubules in the axonemes of trypanosomes. *Journal of Cell Science* 119, 2405–2413.

997 Gambarotto, D., Zwettler, F. U., Le Guennec, M., Schmidt-Cernohorska, M., Fortun, D.,
998 Borgers, S., Heine, J., Schloetel, J.-G., Reuss, M., Unser, M., et al. (2019). Imaging
999 cellular ultrastructures using expansion microscopy (U-ExM). *Nat Methods* 16, 71–74.

1000 González, C., Tavosanis, G. and Mollinari, C. (1998). Centrosomes and microtubule
1001 organisation during *Drosophila* development. *Journal of Cell Science* 111, 2697–2706.

1002 Goodenough, U. W. and StClair, H. S. (1975). BALD-2: a mutation affecting the formation of
1003 doublet and triplet sets of microtubules in Chlamydomonas reinhardtii. *Journal of Cell*
1004 *Biology* 66, 480–491.

1005 Guichard, P. and Gönczy, P. (2016). Basal body structure in Trichonympha. *Cilia* 5, 9.

1006 Guichard, P., Desfosses, A., Maheshwari, A., Hachet, V., Dietrich, C., Brune, A., Ishikawa, T.,
1007 Sachse, C. and Gönczy, P. (2012). Cartwheel Architecture of *Trichonympha* Basal Body.
1008 *Science* 337, 553–553.

1009 Guichard, P., Laporte, M. H. and Hamel, V. (2023). The centriolar tubulin code. *Seminars in Cell*
1010 *& Developmental Biology* 137, 16–25.

1011 Hamel, V., Steib, E., Hamelin, R., Armand, F., Borgers, S., Flückiger, I., Busso, C., Olieric, N.,
1012 Sorzano, C. O. S., Steinmetz, M. O., et al. (2017). Identification of Chlamydomonas
1013 Central Core Centriolar Proteins Reveals a Role for Human WDR90 in Ciliogenesis.
1014 *Current Biology* 27, 2486-2498.e6.

1015 Hatzopoulos, G. N., Erat, M. C., Cutts, E., Rogala, K. B., Slater, L. M., Stansfeld, P. J. and
1016 Vakonakis, I. (2013). Structural Analysis of the G-Box Domain of the Microcephaly
1017 Protein CPAP Suggests a Role in Centriole Architecture. *Structure* 21, 2069–2077.

1018 Hilbert, M., Noga, A., Frey, D., Hamel, V., Guichard, P., Kraatz, S. H. W., Pfreundschuh, M.,
1019 Hosner, S., Flückiger, I., Jaussi, R., et al. (2016). SAS-6 engineering reveals
1020 interdependence between cartwheel and microtubules in determining centriole
1021 architecture. *Nat Cell Biol* 18, 393–403.

1022 Huttlin, E. L., Bruckner, R. J., Paulo, J. A., Cannon, J. R., Ting, L., Baltier, K., Colby, G.,
1023 Gebreab, F., Gygi, M. P., Parzen, H., et al. (2017). Architecture of the human
1024 interactome defines protein communities and disease networks. *Nature* 545, 505–509.

1025 Huttlin, E. L., Bruckner, R. J., Navarrete-Perea, J., Cannon, J. R., Baltier, K., Gebreab, F., Gygi,
1026 M. P., Thornock, A., Zarraga, G., Tam, S., et al. (2021). Dual proteome-scale networks
1027 reveal cell-specific remodeling of the human interactome. *Cell* 184, 3022-3040.e28.

1028 Izquierdo, D., Wang, W.-J., Uryu, K. and Tsou, M.-F. B. (2014). Stabilization of Cartwheel-less
1029 Centrioles for Duplication Requires CEP295-Mediated Centriole-to-Centrosome
1030 Conversion. *Cell Reports* 8, 957–965.

1031 Junker, A. D., Woodhams, L. G., Soh, A. W. J., O'Toole, E. T., Bayly, P. V. and Pearson, C. G.
1032 (2022). Basal bodies bend in response to ciliary forces. *MBoC* 33, ar146.

1033 Kann, M., Soues, S., Levilliers, N. and Fouquet, J. (2003). Glutamylated tubulin: Diversity of
1034 expression and distribution of isoforms. *Cell Motil. Cytoskeleton* 55, 14–25.

1035 Klena, N., Le Guennec, M., Tassin, A., Van Den Hoek, H., Erdmann, P. S., Schaffer, M.,
1036 Geimer, S., Aeschlimann, G., Kovacik, L., Sadian, Y., et al. (2020). Architecture of the
1037 centriole cartwheel-containing region revealed by cryo-electron tomography. *The EMBO*
1038 *Journal* 39, e106246.

1039 Kleylein-Sohn, J., Westendorf, J., Le Clech, M., Habedanck, R., Stierhof, Y.-D. and Nigg, E. A.
1040 (2007). Plk4-Induced Centriole Biogenesis in Human Cells. *Developmental Cell* 13, 190–
1041 202.

1042 Kong, D., Sahabandu, N., Sullenberger, C., Vásquez-Limeta, A., Luvsanjav, D., Lukasik, K. and
1043 Loncarek, J. (2020). Prolonged mitosis results in structurally aberrant and over-
1044 elongated centrioles. *Journal of Cell Biology* 219, e201910019.

1045 Kong, D., Luvsanjav, D. and Loncarek, J. (2024). Immunolabel-First-Expand-Later Expansion
1046 Microscopy Approach Using Stable STED Dyes. *Methods Mol Biol* 2725, 89–101.

1047 Kraatz, S., Guichard, P., Obbineni, J. M., Olieric, N., Hatzopoulos, G. N., Hilbert, M., Sen, I.,
1048 Missimer, J., Gönczy, P. and Steinmetz, M. O. (2016). The Human Centriolar Protein
1049 CEP135 Contains a Two-Stranded Coiled-Coil Domain Critical for Microtubule Binding.
1050 *Structure* 24, 1358–1371.

1051 Kumar, D., Rains, A., Herranz-Pérez, V., Lu, Q., Shi, X., Swaney, D. L., Stevenson, E., Krogan,
1052 N. J., Huang, B., Westlake, C., et al. (2021). A ciliopathy complex builds distal
1053 appendages to initiate ciliogenesis. *Journal of Cell Biology* 220, e202011133.

1054 Laporte, M. H., Bouhlel, I. B., Bertiaux, E., Morrison, C. G., Giroud, A., Borgers, S., Azimzadeh,
1055 J., Bornens, M., Guichard, P., Paoletti, A., et al. (2022). Human SFI1 and Centrin form a
1056 complex critical for centriole architecture and ciliogenesis. *The EMBO Journal* 41,
1057 e112107.

1058 Laporte, M. H., Gambarotto, D., Bertiaux, É., Bournonville, L., Louvel, V., Nunes, J. M., Borgers,
1059 S., Hamel, V. and Guichard, P. (2024). Time-series reconstruction of the molecular
1060 architecture of human centriole assembly. *Cell* 187, 2158-2174.e19.

1061 Le Borgne, P., Greibill, L., Laporte, M. H., Lemullois, M., Bouhouche, K., Temagoult, M.,
1062 Rosnet, O., Le Guennec, M., Lignières, L., Chevreux, G., et al. (2022). The evolutionary
1063 conserved proteins CEP90, FOPNL, and OFD1 recruit centriolar distal appendage
1064 proteins to initiate their assembly. *PLoS Biol* 20, e3001782.

1065 Le Guennec, M., Klena, N., Gambarotto, D., Laporte, M. H., Tassin, A.-M., Van Den Hoek, H.,
1066 Erdmann, P. S., Schaffer, M., Kovacik, L., Borgers, S., et al. (2020). A helical inner
1067 scaffold provides a structural basis for centriole cohesion. *Sci. Adv.* 6, eaaz4137.

1068 LeGuennec, M., Klena, N., Aeschlimann, G., Hamel, V. and Guichard, P. (2021). Overview of
1069 the centriole architecture. *Current Opinion in Structural Biology* 66, 58–65.

1070 Lin, Y.-C., Chang, C.-W., Hsu, W.-B., Tang, C.-J. C., Lin, Y.-N., Chou, E.-J., Wu, C.-T. and
1071 Tang, T. K. (2013a). Human microcephaly protein CEP135 binds to hSAS-6 and CPAP,
1072 and is required for centriole assembly. *EMBO J* 32, 1141–1154.

1073 Lin, Y.-N., Wu, C.-T., Lin, Y.-C., Hsu, W.-B., Tang, C.-J. C., Chang, C.-W. and Tang, T. K.
1074 (2013b). CEP120 interacts with CPAP and positively regulates centriole elongation.
1075 *Journal of Cell Biology* 202, 211–219.

1076 Mahecic, D., Gambarotto, D., Douglass, K. M., Fortun, D., Banterle, N., Ibrahim, K. A., Le
1077 Guennec, M., Gönczy, P., Hamel, V., Guichard, P., et al. (2020). Homogeneous
1078 multifocal excitation for high-throughput super-resolution imaging. *Nat Methods* 17, 726–
1079 733.

1080 Mahjoub, M. R., Xie, Z. and Stearns, T. (2010). Cep120 is asymmetrically localized to the
1081 daughter centriole and is essential for centriole assembly. *Journal of Cell Biology* 191,
1082 331–346.

1083 Pelletier, L., O'Toole, E., Schwager, A., Hyman, A. A. and Müller-Reichert, T. (2006). Centriole
1084 assembly in Caenorhabditis elegans. *Nature* 444, 619–623.

1085 Pierron, M., Woglar, A., Busso, C., Jha, K., Mikeladze-Dvali, T., Croisier, M. and Gönczy, P.
1086 (2023). Centriole elimination during *Caenorhabditis elegans* oogenesis initiates with loss
1087 of the central tube protein SAS -1. *The EMBO Journal* 42, e115076.

1088 Pimenta-Marques, A., Bento, I., Lopes, C. a. M., Duarte, P., Jana, S. C. and Bettencourt-Dias,
1089 M. (2016). A mechanism for the elimination of the female gamete centrosome in
1090 Drosophila melanogaster. *Science* 353, aaf4866.

1091 Ross, I., Clarissa, C., Giddings, T. H. and Winey, M. (2013). ε-tubulin is essential in
1092 *Tetrahymena thermophila* for the assembly and stability of basal bodies. *Journal of Cell*
1093 *Science* jcs.128694.

1094 Sahabandu, N., Kong, D., Magidson, V., Nanjundappa, R., Sullenberger, C., Mahjoub, M. R.
1095 and Loncarek, J. (2019). Expansion microscopy for the analysis of centrioles and cilia.
1096 *Journal of Microscopy* 276, 145–159.

1097 Sala, C., Würtz, M., Atorino, E. S., Neuner, A., Partscht, P., Hoffmann, T., Eustermann, S. and
1098 Schiebel, E. (2024). An interaction network of inner centriole proteins organised by
1099 POC1A-POC1B heterodimer crosslinks ensures centriolar integrity. *Nat Commun* 15,
1100 9857.

1101 Schindelin, J., Arganda-Carreras, I., Frise, E., Kaynig, V., Longair, M., Pietzsch, T., Preibisch,
1102 S., Rueden, C., Saalfeld, S., Schmid, B., et al. (2012). Fiji: an open-source platform for
1103 biological-image analysis. *Nat Methods* 9, 676–682.

1104 Schweizer, N., Haren, L., Dutto, I., Viais, R., Lacasa, C., Merdes, A. and Lüders, J. (2021). Sub-
1105 centrosomal mapping identifies augmin-γTuRC as part of a centriole-stabilizing scaffold.
1106 *Nat Commun* 12, 6042.

1107 Sharma, A., Aher, A., Dynes, N. J., Frey, D., Katrukha, E. A., Jaussi, R., Grigoriev, I., Croisier,
1108 M., Kammerer, R. A., Akhmanova, A., et al. (2016). Centriolar CPAP/SAS-4 Imparts
1109 Slow Processive Microtubule Growth. *Developmental Cell* 37, 362–376.

1110 Spektor, A., Tsang, W. Y., Khoo, D. and Dynlacht, B. D. (2007). Cep97 and CP110 Suppress a
1111 Cilia Assembly Program. *Cell* 130, 678–690.

1112 Steib, E., Laporte, M. H., Gambarotto, D., Olieric, N., Zheng, C., Borgers, S., Olieric, V., Le
1113 Guennec, M., Koll, F., Tassin, A.-M., et al. (2020). WDR90 is a centriolar microtubule
1114 wall protein important for centriole architecture integrity. *eLife* 9, e57205.

1115 Sullenberger, C., Vasquez-Limeta, A., Kong, D. and Loncarek, J. (2020). With Age Comes
1116 Maturity: Biochemical and Structural Transformation of a Human Centriole in the Making.
1117 *Cells* 9, 1429.

1118 Tischer, J., Carden, S. and Gergely, F. (2021). Accessorizing the centrosome: new insights into
1119 centriolar appendages and satellites. *Current Opinion in Structural Biology* 66, 148–155.

1120 Uphoff, C. C. and Drexler, H. G. (2011). Detecting Mycoplasma Contamination in Cell Cultures
1121 by Polymerase Chain Reaction. In *Cancer Cell Culture* (ed. Cree, I. A.), pp. 93–103.
1122 Totowa, NJ: Humana Press.

1123 Van Dijk, J., Rogowski, K., Miro, J., Lacroix, B., Eddé, B. and Janke, C. (2007). A Targeted
1124 Multienzyme Mechanism for Selective Microtubule Polyglutamylation. *Molecular Cell* 26,
1125 437–448.

1126 Vásquez-Limeta, A., Lukasik, K., Kong, D., Sullenberger, C., Luvsanjav, D., Sahabandu, N.,
1127 Chari, R. and Loncarek, J. (2022). CPAP insufficiency leads to incomplete centrioles that
1128 duplicate but fragment. *Journal of Cell Biology* 221, e202108018.

1129 Wang, J. T. and Stearns, T. (2017). The ABCs of Centriole Architecture: The Form and Function
1130 of Triplet Microtubules. *Cold Spring Harb Symp Quant Biol* 82, 145–155.

1131 Wang, W.-J., Acehan, D., Kao, C.-H., Jane, W.-N., Uryu, K. and Tsou, M.-F. B. (2015). De novo
1132 centriole formation in human cells is error-prone and does not require SAS-6 self-
1133 assembly. *eLife* 4, e10586.

1134 Wang, J. T., Kong, D., Hoerner, C. R., Loncarek, J. and Stearns, T. (2017). Centriole triplet
1135 microtubules are required for stable centriole formation and inheritance in human cells.
1136 *eLife* 6, e29061.

1137 Woglar, A., Pierron, M., Schneider, F. Z., Jha, K., Busso, C. and Gönczy, P. (2022). Molecular
1138 architecture of the C. elegans centriole. *PLoS Biol* 20, e3001784.

1139 Zhang, Y., Vanoli, F., LaRocque, J. R., Krawczyk, P. M. and Jasin, M. (2014). Biallelic targeting
1140 of expressed genes in mouse embryonic stem cells using the Cas9 system. *Methods* 69,
1141 171–178.

1142

Figure 1

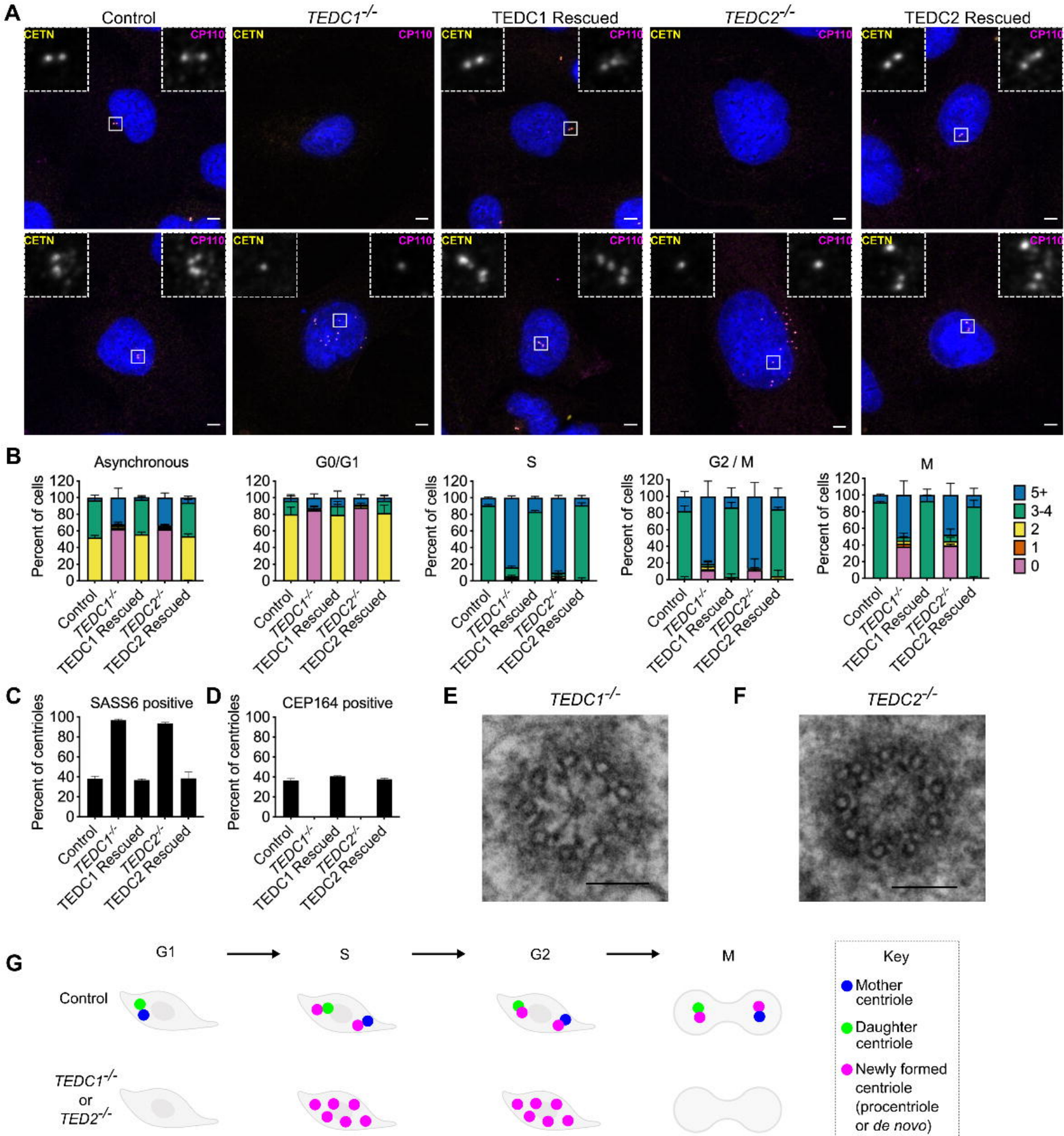
A
Control
TEDC1 Rescued
TEDC2 Rescued
CETN
CP110
B
Asynchronous
G0/G1
S
G2 / M
M
Percent of cells
5+
3-4
2
1
0
Control
TEDC1 Rescued
TEDC2 Rescued
C
SASS6 positive
Percent of centrioles
D
CEP164 positive
E
F
G
G1
S
G2
M
Key
Mother centriole
Daughter centriole
Newly formed centriole (procentriole or de novo)

Figure 1 - Supp 1

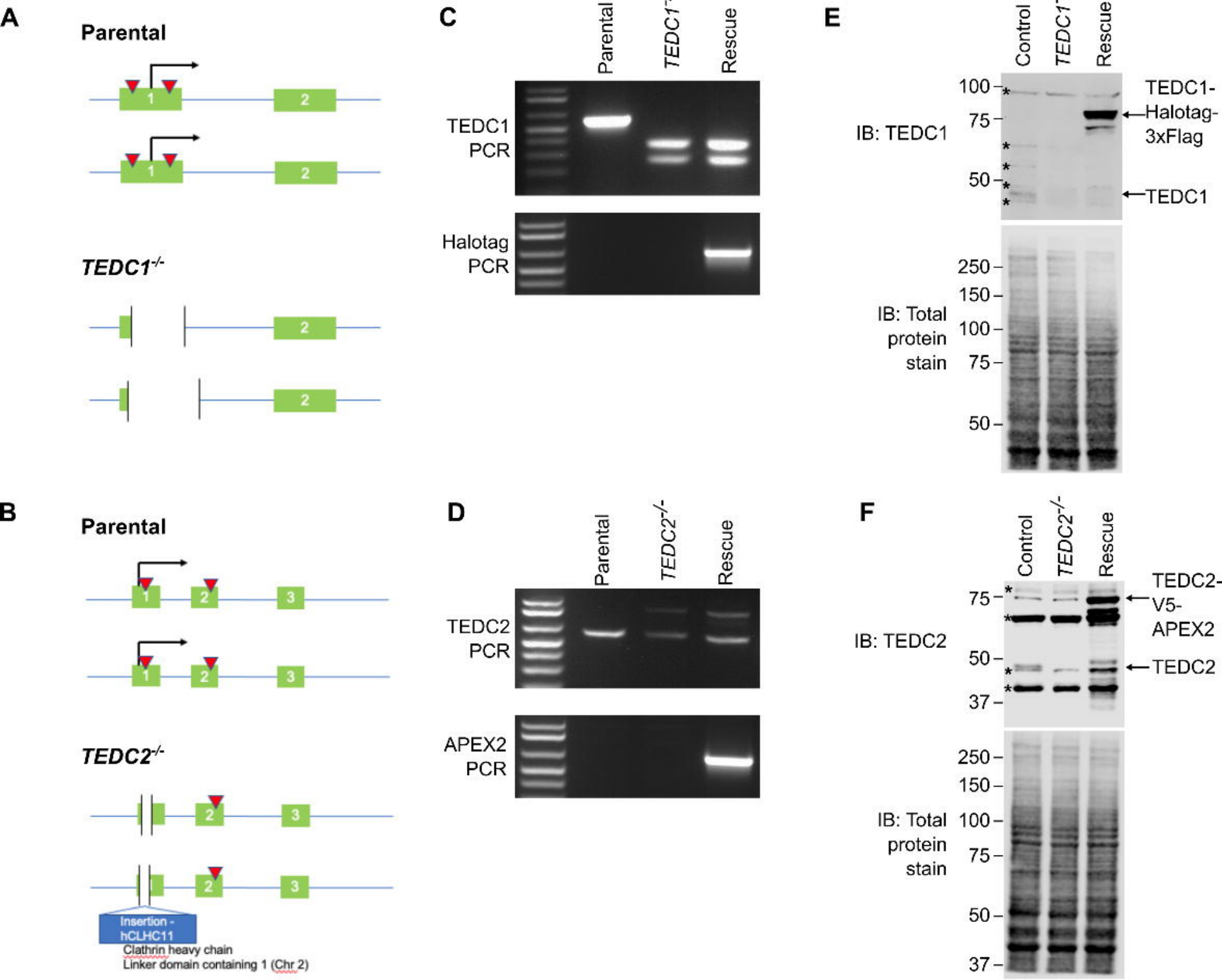

Fig 1 - Supp 2

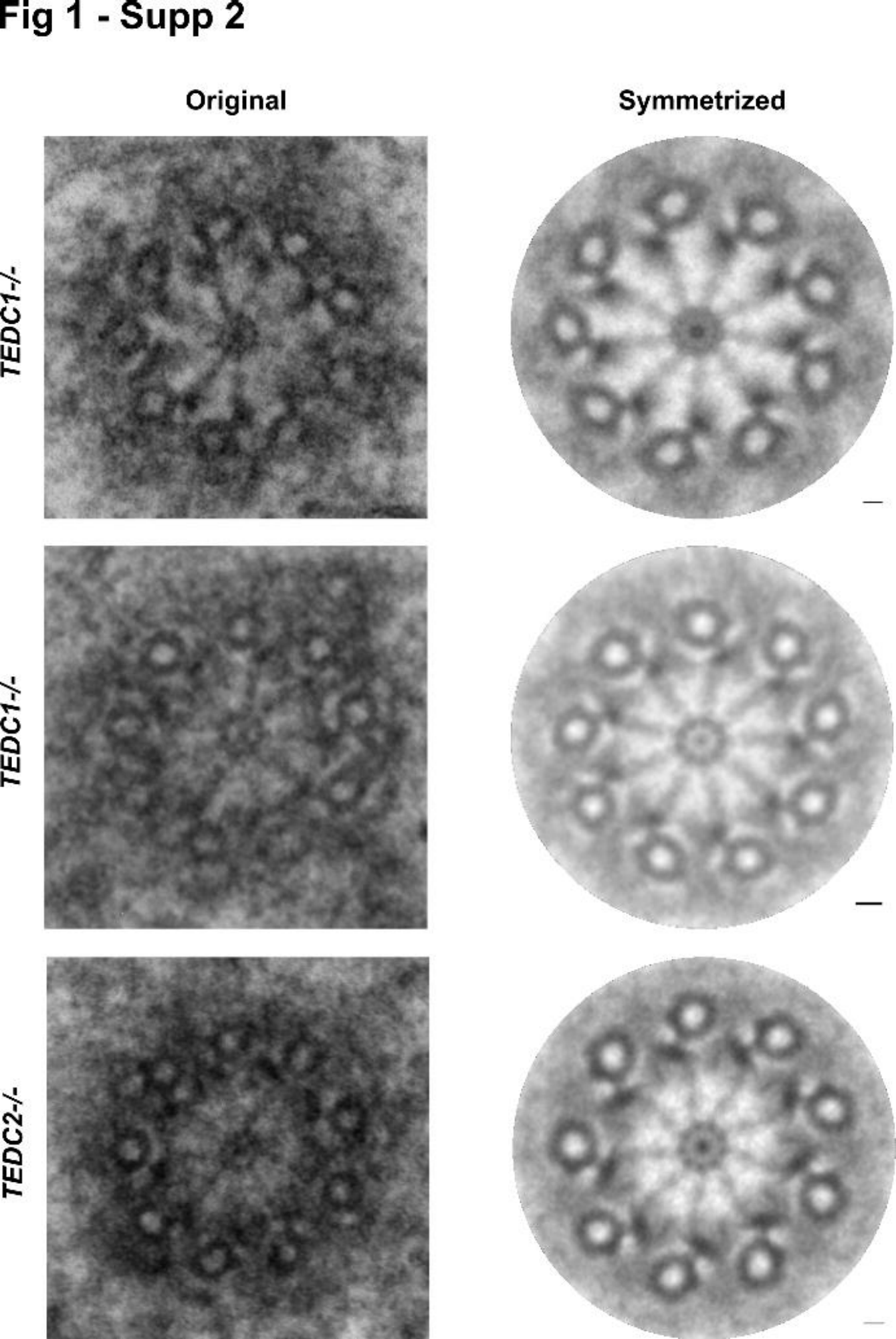

Figure 2

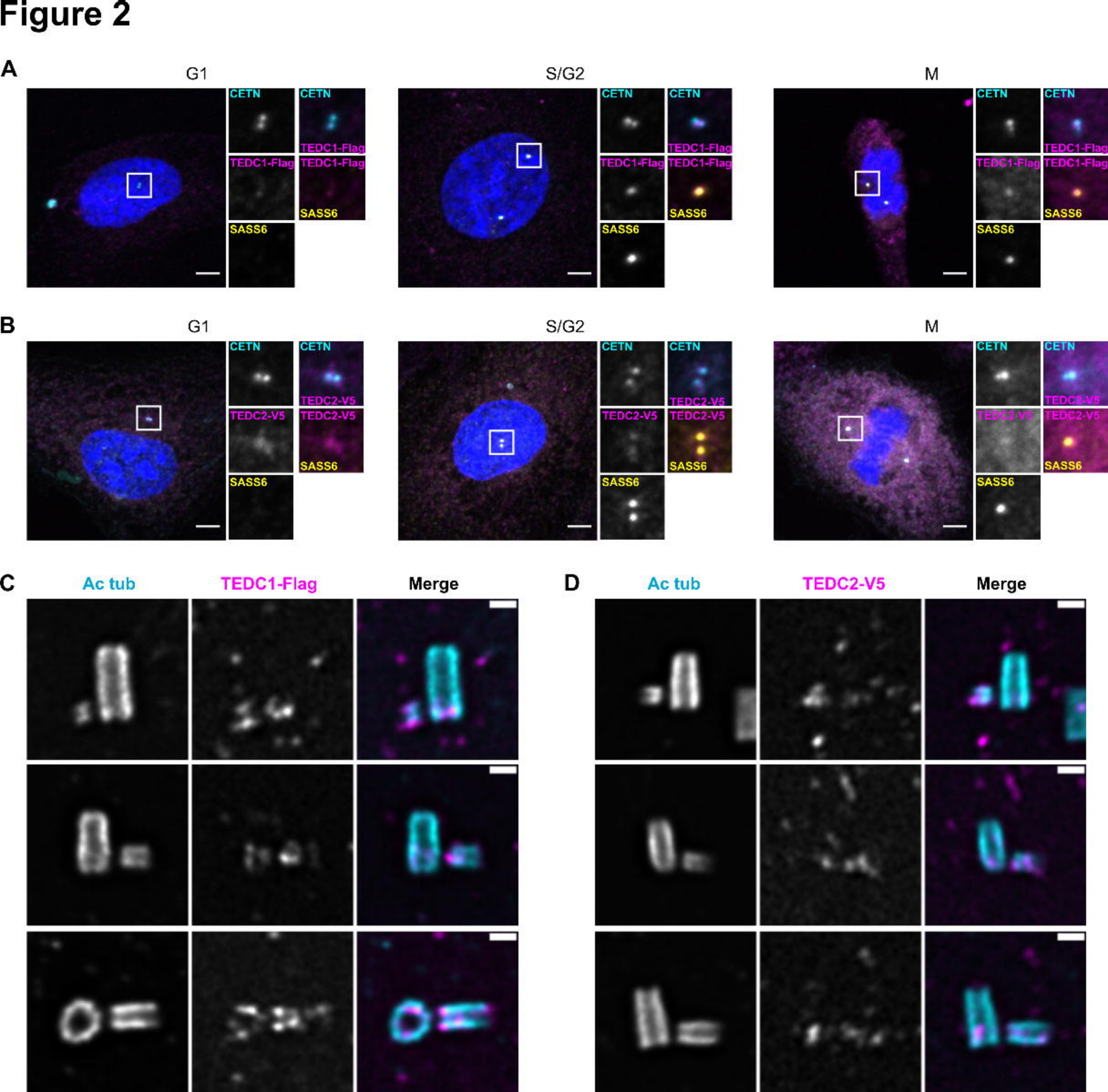
A
G1
S/G2
M
CETN
TEDC1-Flag
SASS6
B
G1
S/G2
M
CETN
TEDC2-V5
SASS6
C
Ac tub
TEDC1-Flag
Merge
D
Ac tub
TEDC2-V5
Merge

Figure 2 - Supp 1

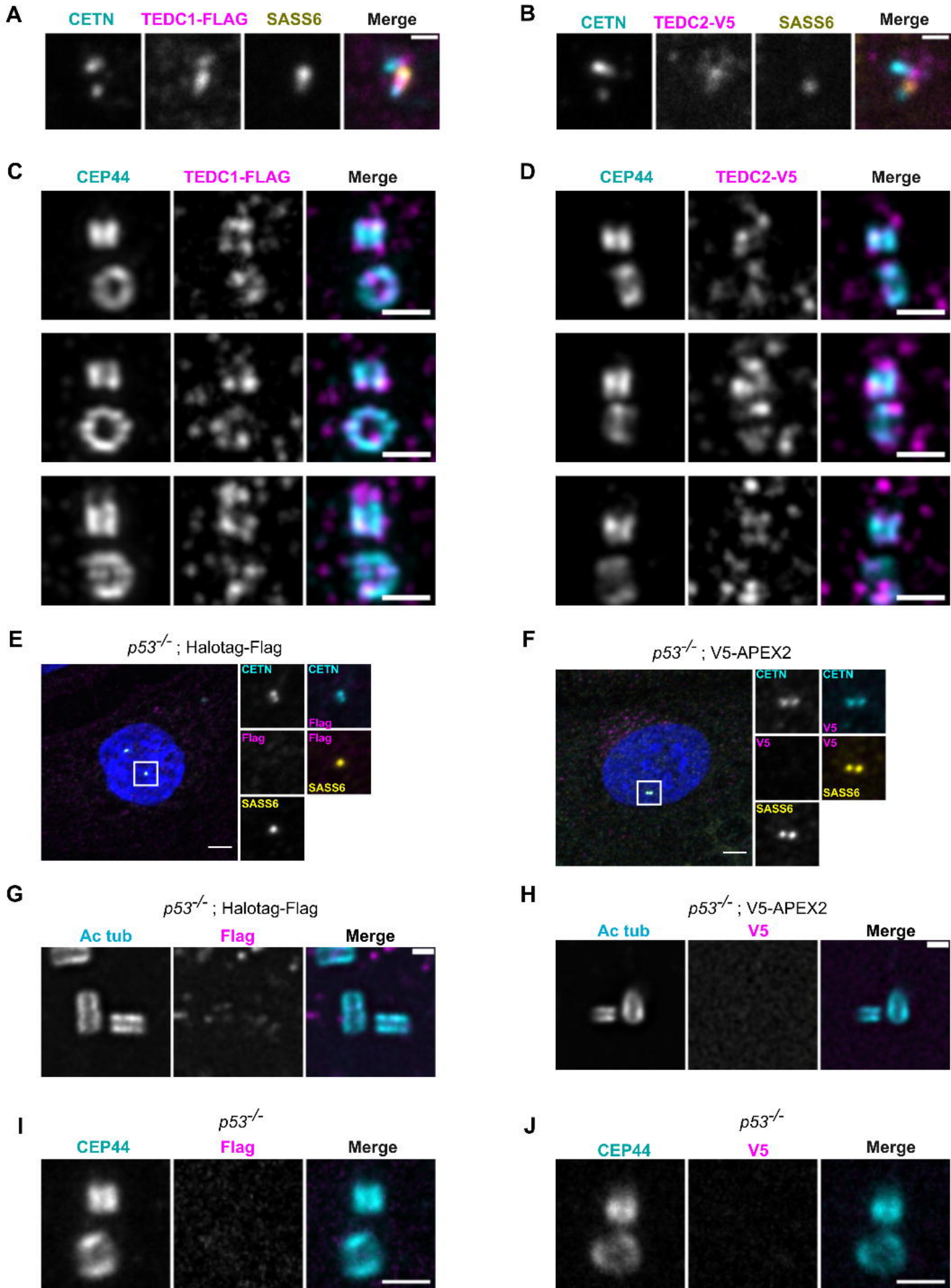

Figure 3

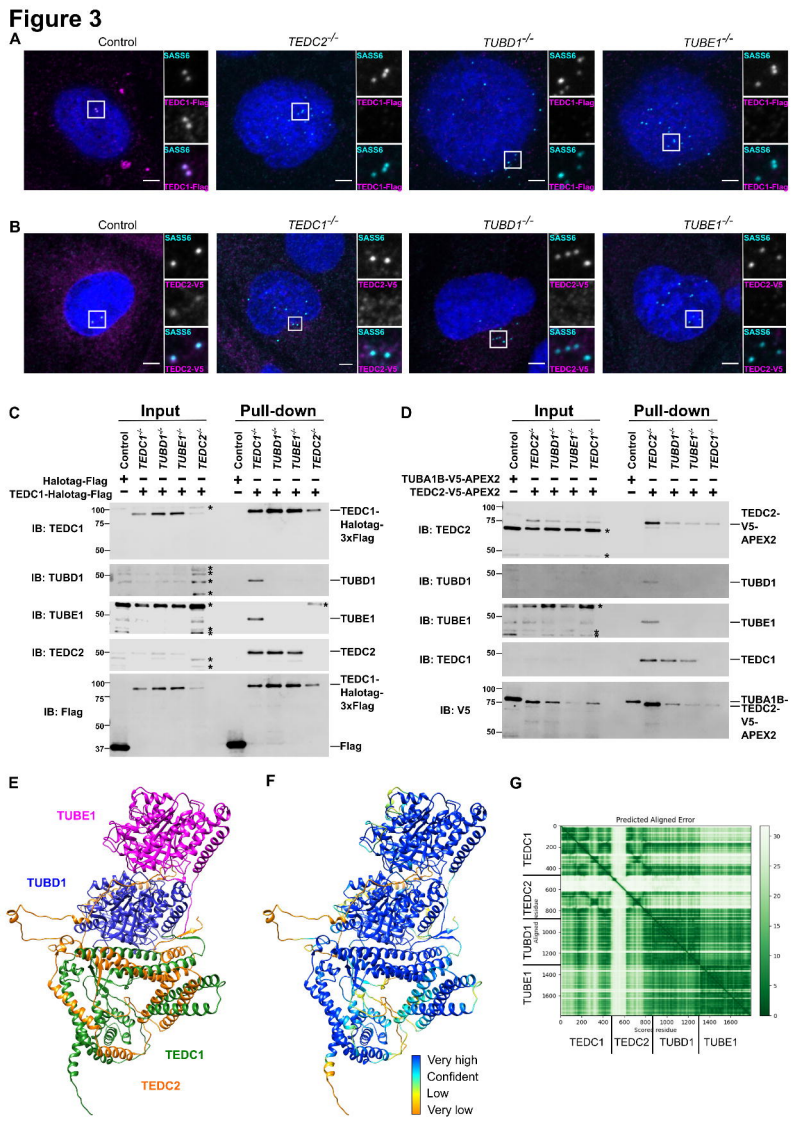
A
Control
TEDC2-/-
TUBD1-/-
TUBE1-/-
SASS6
TEDC1-Flag
B
Control
TEDC1-/-
TUBD1-/-
TUBE1-/-
SASS6
TEDC2-V5
C
Input
Pull-down
Halotag-Flag
TEDC1-Halotag-Flag
Control
TEDC1-/-
TUBD1-/-
TUBE1-/-
TEDC2-/-
IB: TEDC1
IB: TUBD1
IB: TUBE1
IB: TEDC2
IB: Flag
TEDC1-Halotag-3xFlag
TUBD1
TUBE1
TEDC2
Flag
D
Input
Pull-down
TUBA1B-V5-APEX2
TEDC2-V5-APEX2
Control
TEDC2-/-
TUBD1-/-
TUBE1-/-
TEDC1-/-
IB: TEDC2
IB: TUBD1
IB: TUBE1
IB: TEDC1
IB: V5
TEDC2-V5-APEX2
TUBD1
TUBE1
TEDC1
TUBA1B-TEDC2-V5-APEX2
E
TUBE1
TUBD1
TEDC1
TEDC2
F
Very high
Confident
Low
Very low
G
Predicted Aligned Error
Aligned residue
Scored residue
TEDC1
TEDC2
TUBD1
TUBE1

Figure 3 - Supp 1

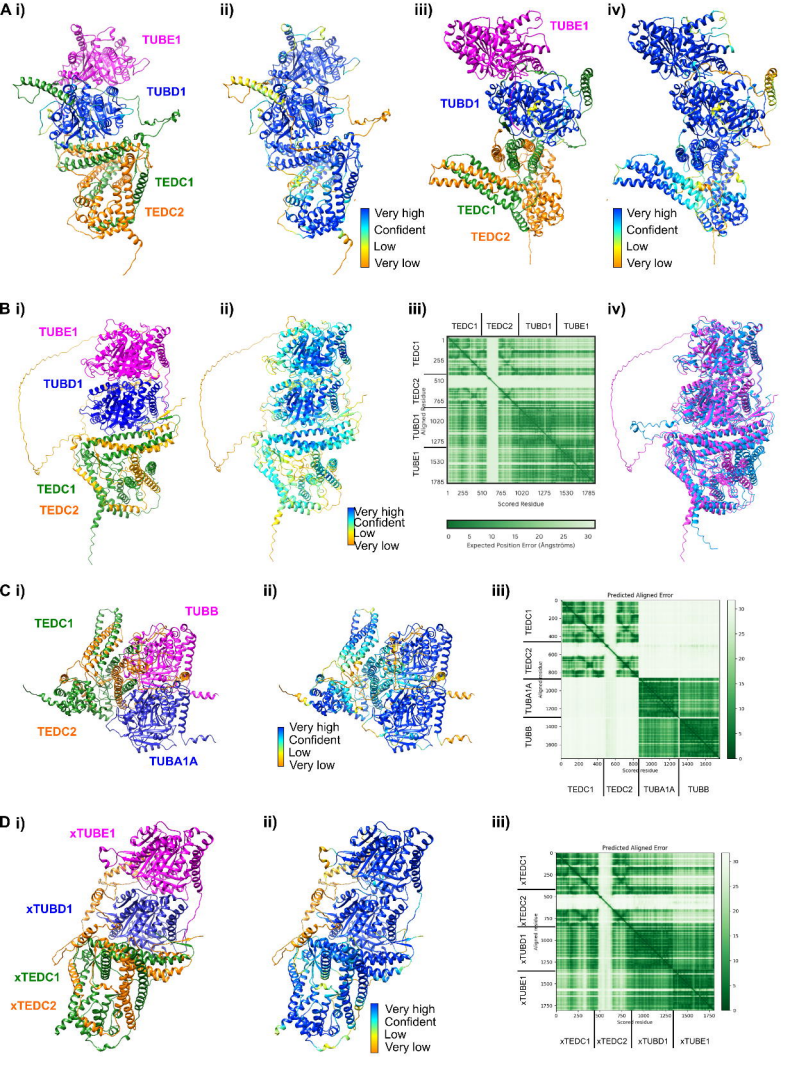

Figure 4

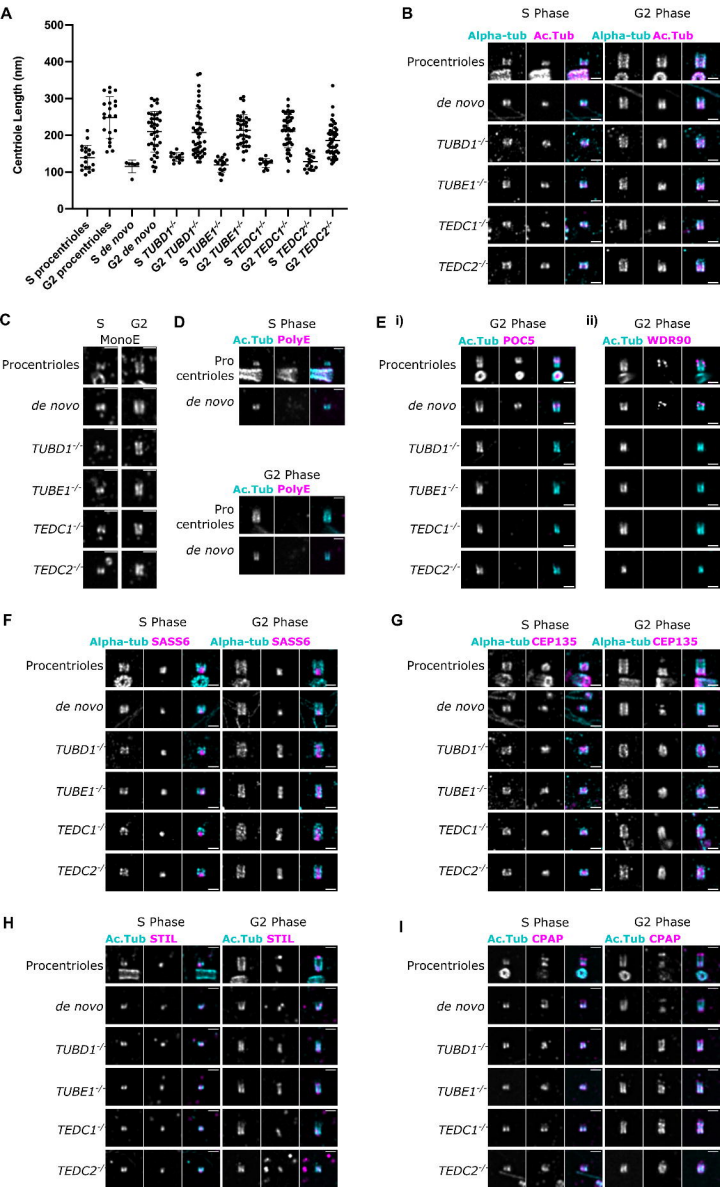
A
Centriole Length (nm)
500
400
300
200
100
0
S procentrioles
G2 procentrioles
S de novo
G2 de novo
S TUBD1-/-
G2 TUBD1-/-
S TUBE1-/-
G2 TUBE1-/-
S TEDC1-/-
G2 TEDC1-/-
S TEDC2-/-
G2 TEDC2-/-
B
S Phase
G2 Phase
Alpha-tub Ac.Tub
Alpha-tub Ac.Tub
Procentrioles
de novo
TUBD1-/-
TUBE1-/-
TEDC1-/-
TEDC2-/-
C
S
G2
MonoE
Procentrioles
de novo
TUBD1-/-
TUBE1-/-
TEDC1-/-
TEDC2-/-
D
S Phase
Ac.Tub PolyE
Pro centrioles
de novo
G2 Phase
Ac.Tub PolyE
Pro centrioles
de novo
E
i)
G2 Phase
Ac.Tub POC5
ii)
G2 Phase
Ac.Tub WDR90
Procentrioles
de novo
TUBD1-/-
TUBE1-/-
TEDC1-/-
TEDC2-/-
F
S Phase
G2 Phase
Alpha-tub SASS6
Alpha-tub SASS6
Procentrioles
de novo
TUBD1-/-
TUBE1-/-
TEDC1-/-
TEDC2-/-
G
S Phase
G2 Phase
Alpha-tub CEP135
Alpha-tub CEP135
Procentrioles
de novo
TUBD1-/-
TUBE1-/-
TEDC1-/-
TEDC2-/-
H
S Phase
G2 Phase
Ac.Tub STIL
Ac.Tub STIL
Procentrioles
de novo
TUBD1-/-
TUBE1-/-
TEDC1-/-
TEDC2-/-
I
S Phase
G2 Phase
Ac.Tub CPAP
Ac.Tub CPAP
Procentrioles
de novo
TUBD1-/-
TUBE1-/-
TEDC1-/-
TEDC2-/-

Figure 4 - Supp 1

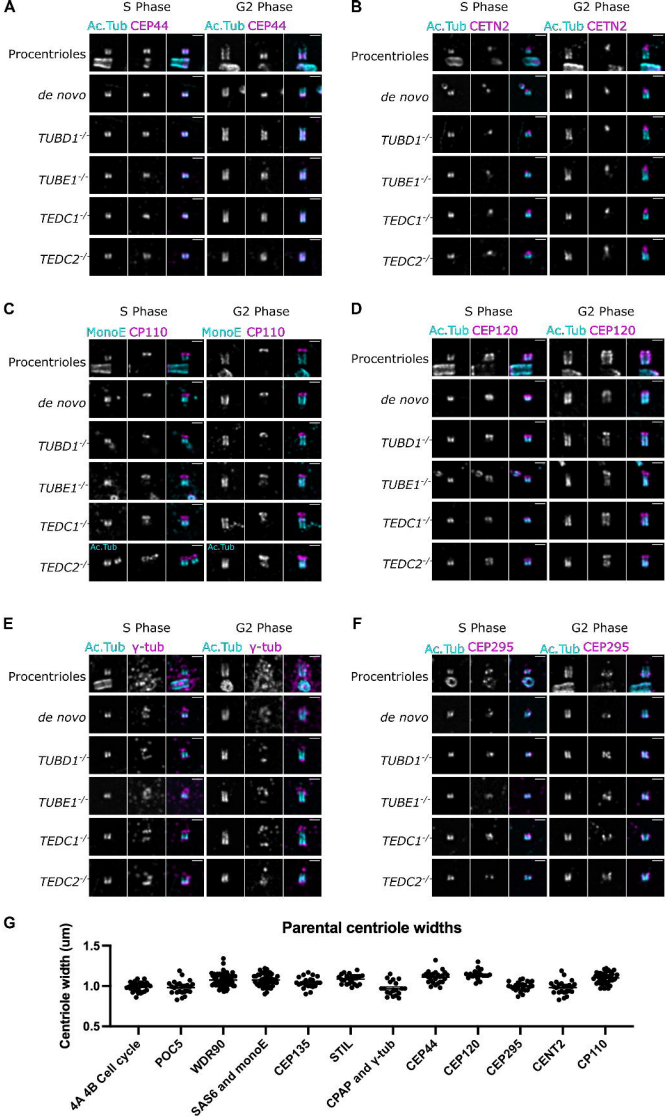

Figure 4 - Supp 2

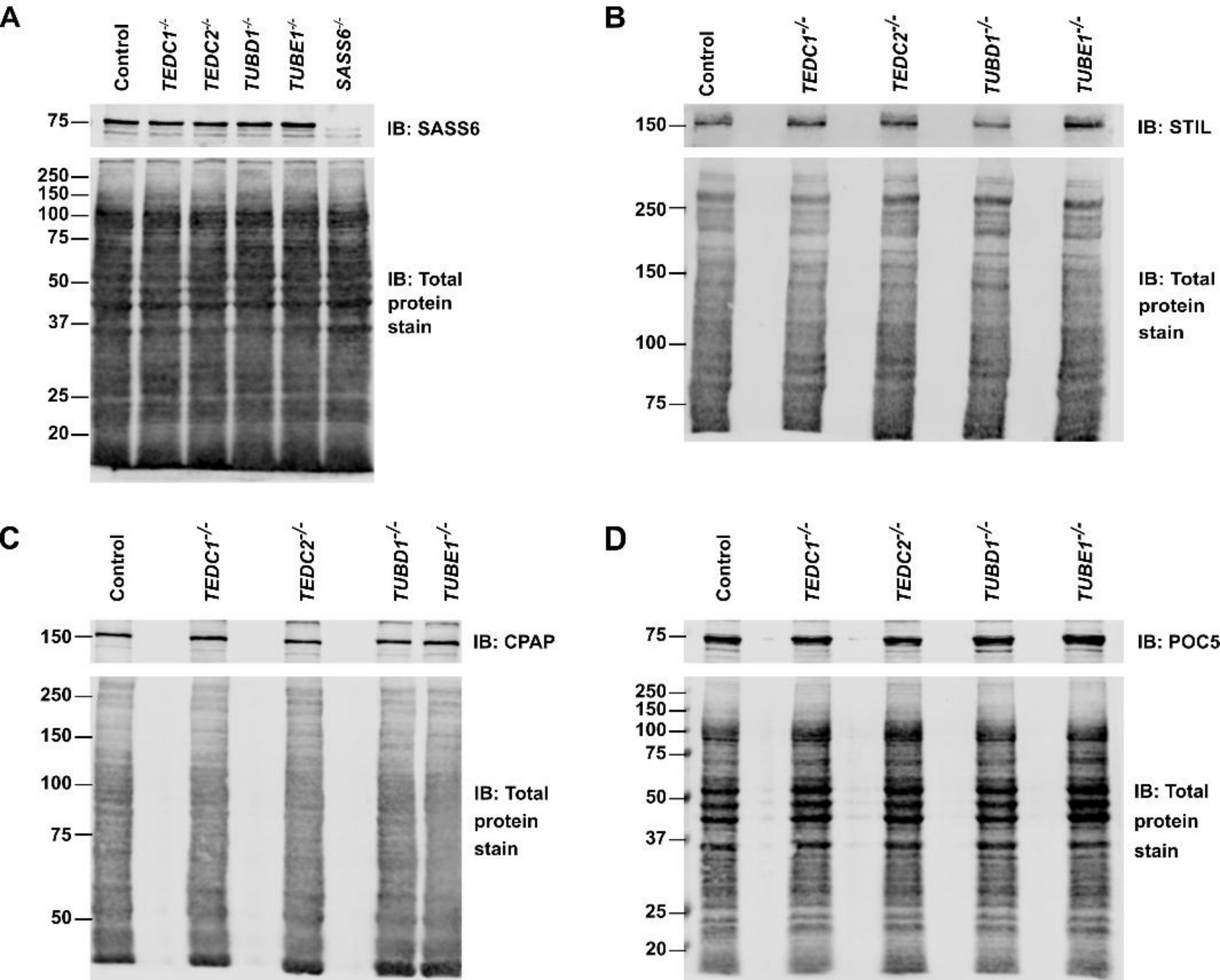

Figure 4 - Supp 3

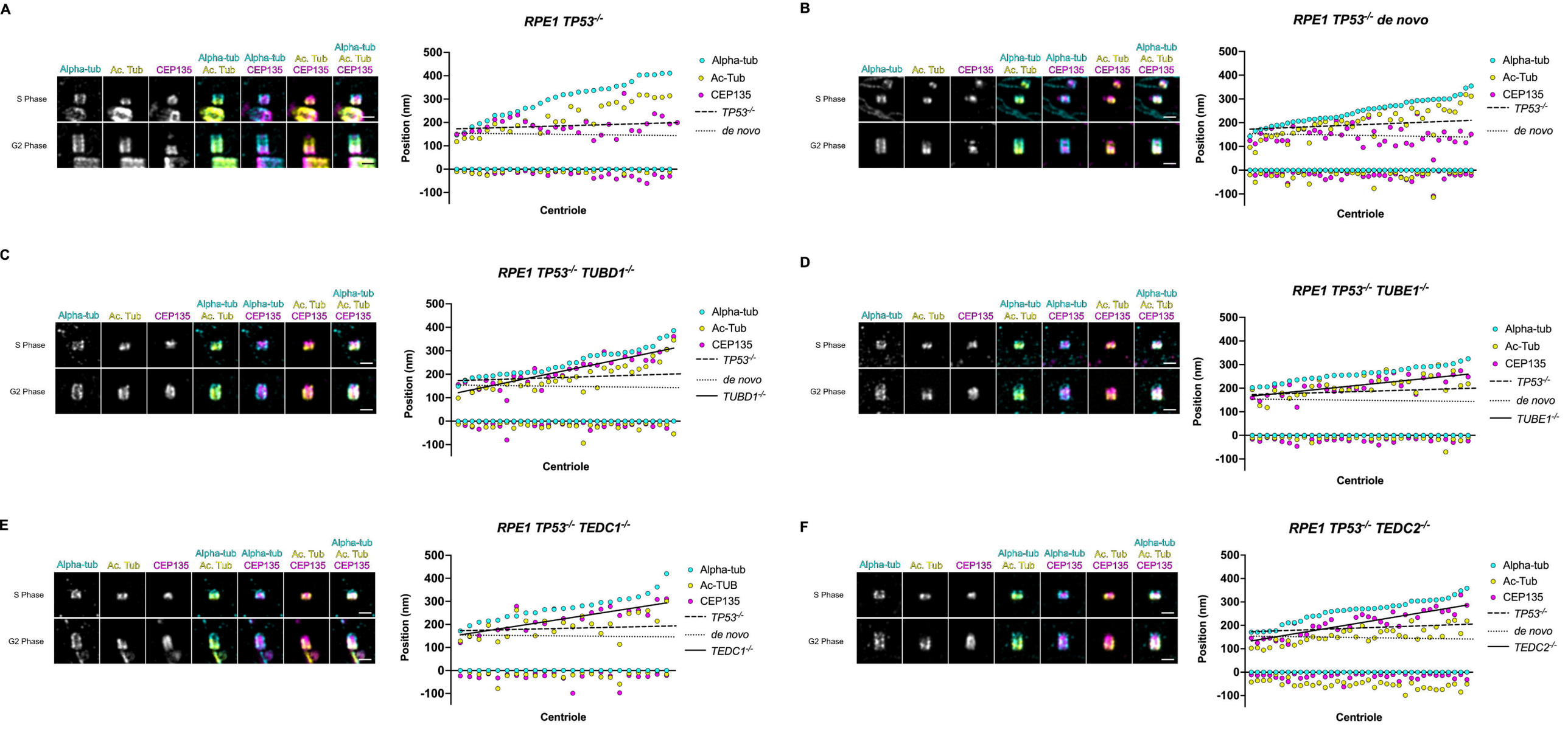

Fig 4 - Supp 4

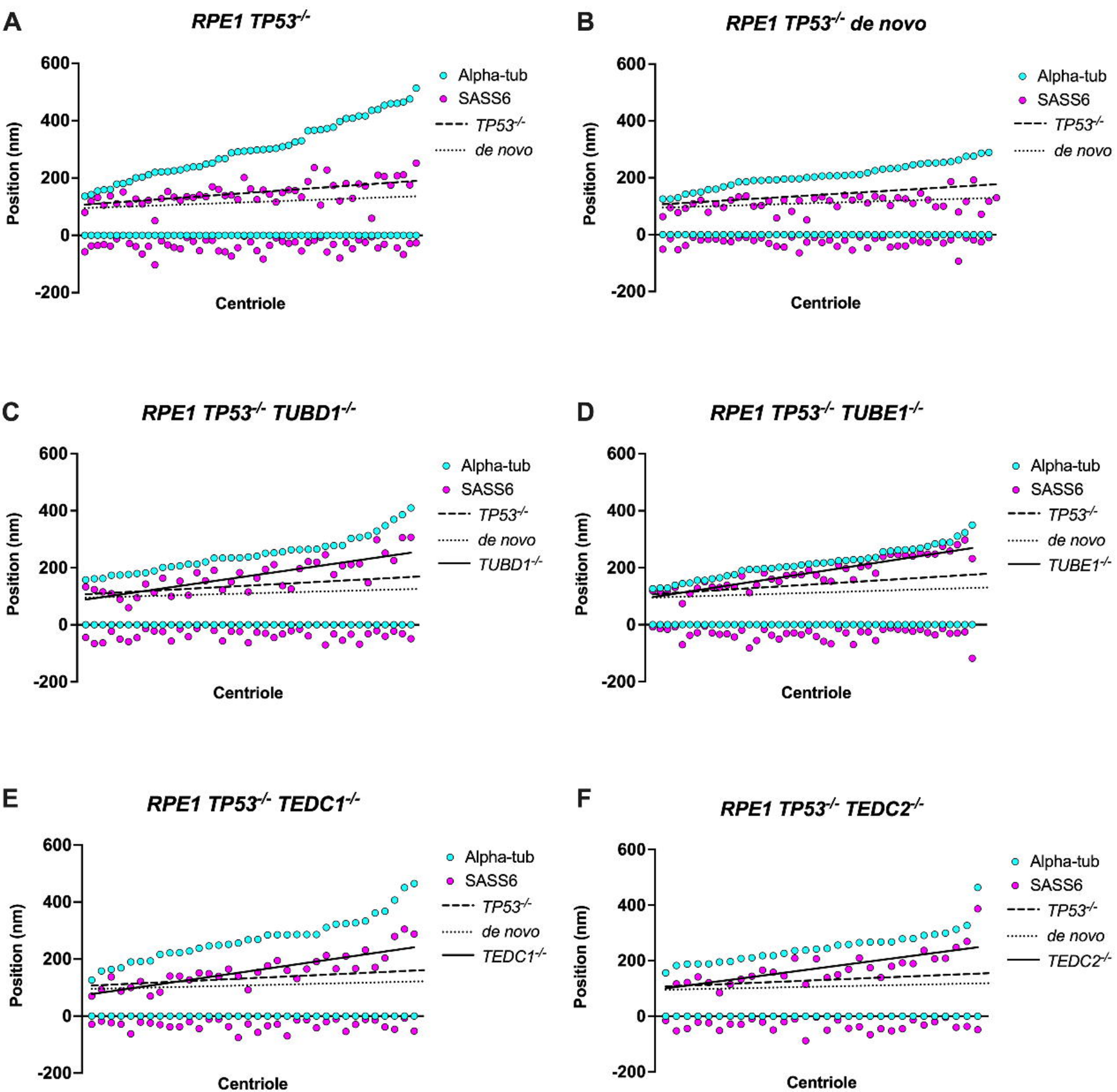
A
RPE1 TP53-/-
B
RPE1 TP53-/- de novo
C
RPE1 TP53-/- TUBD1-/-
D
RPE1 TP53-/- TUBE1-/-
E
RPE1 TP53-/- TEDC1-/-
F
RPE1 TP53-/- TEDC2-/-
Position (nm)
600
400
200
0
-200
Centriole
Alpha-tub
SASS6
TP53-/-
de novo
TUBD1-/-
TUBE1-/-
TEDC1-/-
TEDC2-/-

Fig 4 - Supp 5

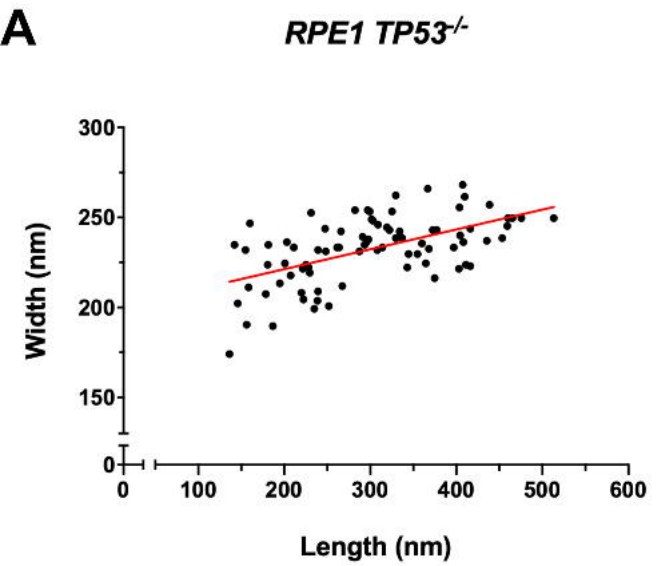
A
RPE1 TP53-/-
Width (nm)
Length (nm)
0
150
200
250
300
0
100
200
300
400
500
600

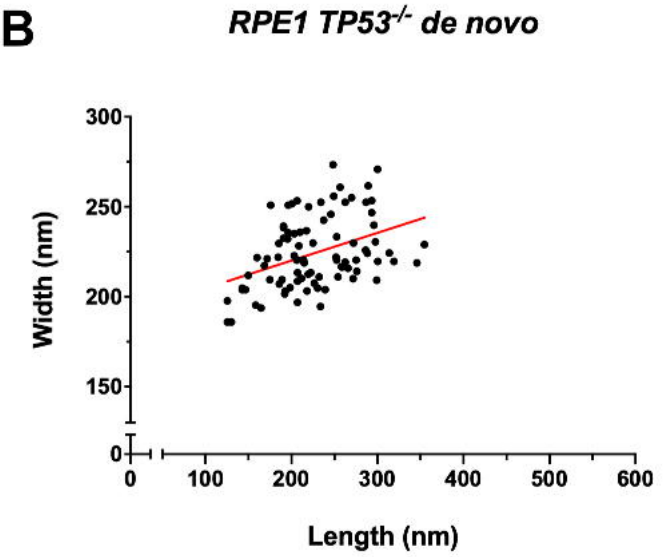
B
RPE1 TP53-/- de novo
Width (nm)
Length (nm)
0
150
200
250
300
0
100
200
300
400
500
600

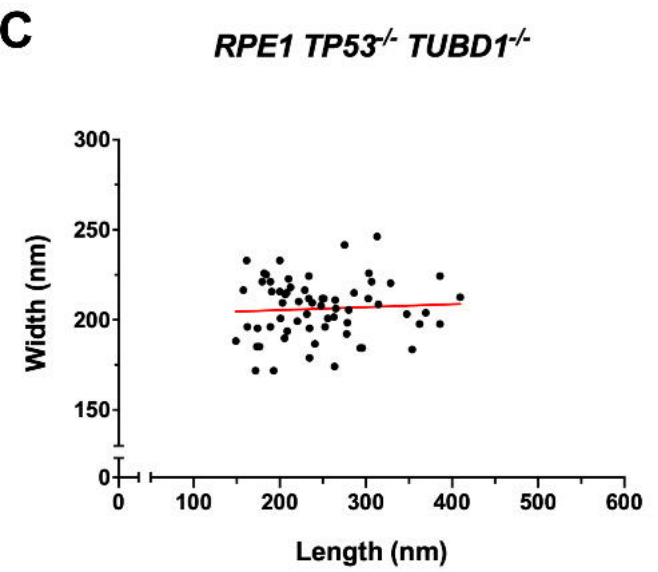
C
RPE1 TP53-/- TUBD1-/-
Width (nm)
Length (nm)
0
150
200
250
300
0
100
200
300
400
500
600

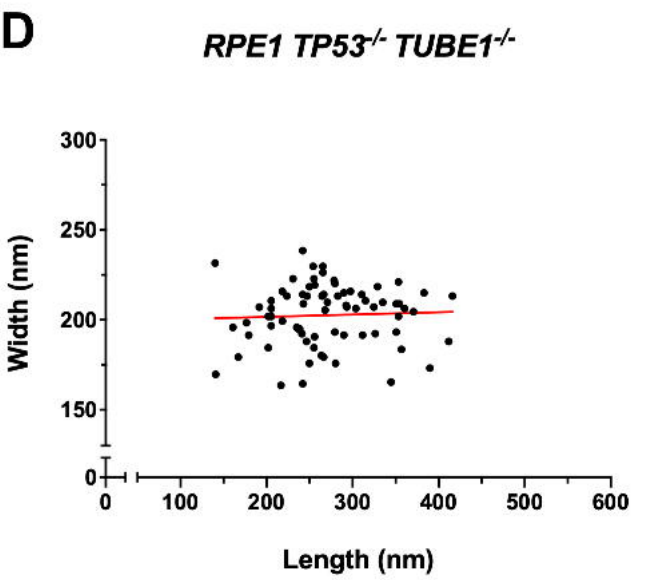
D
RPE1 TP53-/- TUBE1-/-
Width (nm)
Length (nm)
0
150
200
250
300
0
100
200
300
400
500
600

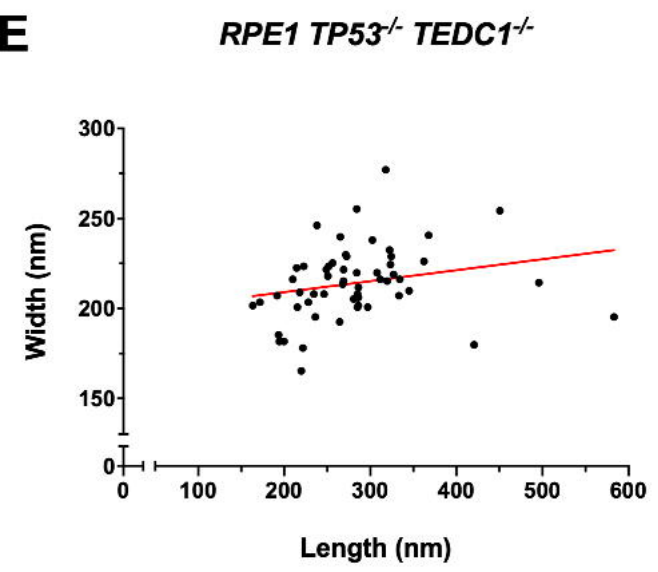
E
RPE1 TP53-/- TEDC1-/-
Width (nm)
Length (nm)
0
150
200
250
300
0
100
200
300
400
500
600

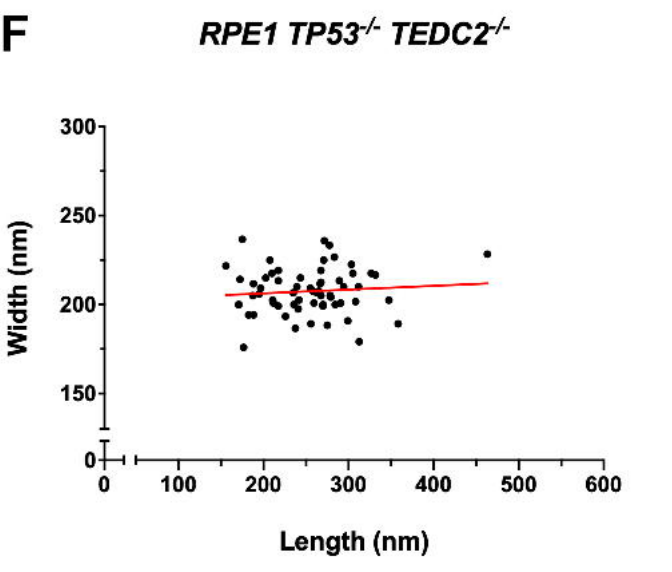
F
RPE1 TP53-/- TEDC2-/-
Width (nm)
Length (nm)
0
150
200
250
300
0
100
200
300
400
500
600

Figure 5

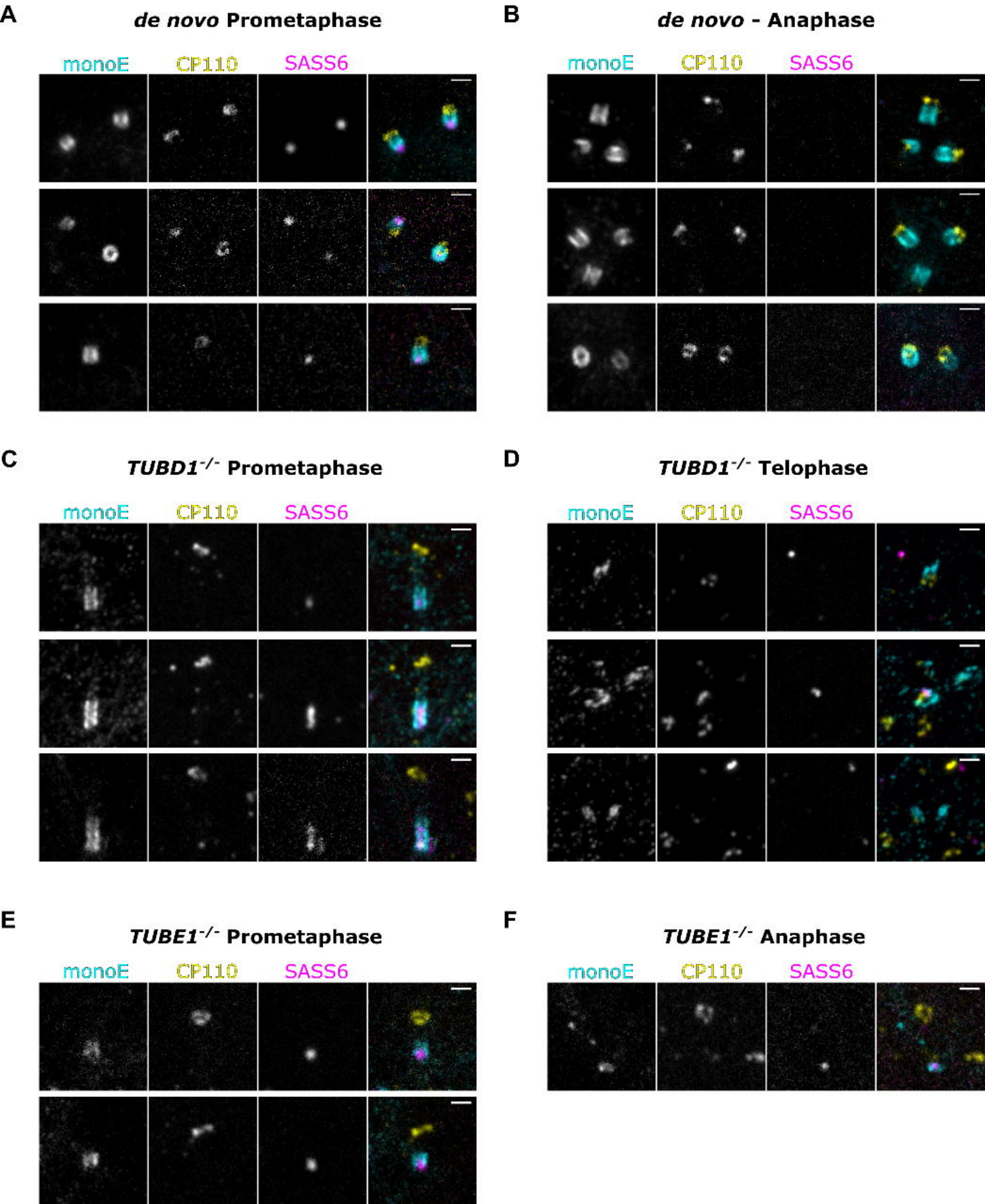
A
de novo Prometaphase
monoE
CP110
SASS6
B
de novo - Anaphase
monoE
CP110
SASS6
C
TUBD1-/- Prometaphase
monoE
CP110
SASS6
D
TUBD1-/- Telophase
monoE
CP110
SASS6
E
TUBE1-/- Prometaphase
monoE
CP110
SASS6
F
TUBE1-/- Anaphase
monoE
CP110
SASS6